PHYSICAL REVIEW D

PARTICLES AND FIELDS

THIRD SERIES, VOLUME 40, NUMBER 1 1 JULY 1989

High-energy photoproduction of $\pi^+\pi^-\pi^0$, K^+K^-, and $p\bar{p}$ states

J. Busenitz,* C. Olszewski,† P. Callahan,‡ G. Gladding, and A. Wattenberg
University of Illinois at Urbana-Champaign, 1110 West Green Street, Urbana, Illinois 61801

M. Binkley, J. Butler, J. Cumalat,§ I. Gaines, M. Gormley, D. Harding,
R. L. Loveless,** and J. Peoples
Fermi National Accelerator Laboratory, Batavia, Illinois 60510

(Received 26 October 1988)

We report measurements from elastic photoproduction of ω's on hydrogen for photon energies between 60 and 225 GeV, elastic ϕ photoproduction on hydrogen between 35 and 165 GeV and on deuterium between 45 and 85 GeV, elastic photoproduction on deuterium of an enhancement at 1.72 GeV/c^2 decaying into K^+K^-, and elastic and inelastic photoproduction on deuterium of $p\bar{p}$ pairs.

I. INTRODUCTION

This paper reports measurements of high-energy photoproduction into the channels $\pi^+\pi^-\pi^0$, K^+K^-, and $p\bar{p}$. To be specific, first, the s and t dependence and angular properties of elastic ω photoproduction on hydrogen have been measured for photon energies between 60 and 225 GeV. The ω was observed via its decay into $\pi^+\pi^-\pi^0$. Second, we have measured the s and t dependence of elastic ϕ photoproduction from hydrogen and deuterium targets. The hydrogen measurement covers the energy range 35–165 GeV; the deuterium measurement is limited to the energy range 45–85 GeV but has very high statistics, making a detailed measurement of the s dependence in this region possible. Our measurements of $(d\sigma/dt)(\gamma p \to \phi p)$ are the first such measurements above 40 GeV. Third, we report on the observation and study of an enhancement at 1.72 GeV/c^2 decaying into K^+K^-. Finally, we have studied both the elastic and inelastic production of $p\bar{p}$ pairs. Upper limits are set on the photoproduction of resonances reported by previous experiments and results of searches for other resonances are given.

The remainder of this paper is organized as follows. Section II describes the relevant features of the beam, detector, and triggers. Results on the photoproduction of the ω, the ϕ, the enhancement at 1.72 GeV/c^2, and $p\bar{p}$ pairs are reported and discussed in Secs. III, IV, V, and VI, respectively. Section VII is a summary.

II. EXPERIMENTAL SETUP

The data were taken in the Fermilab broad-band photon beam by Experiment 401. Photons originated mainly from the decay of secondary π^0's produced by 350-GeV protons incident on beryllium. Noninteracting protons and charged secondaries were swept away by magnets and the ratio of photons to neutral hadrons was enhanced by passing the neutral beam through a liquid-deuterium filter, shown schematically in Fig. 1. (A schematic of the entire beam line, including the liquid-deuterium filter, is shown in Ref. 1.) The resulting neutral beam at the experimental target was about 99% γ's across the energy range of our measurements. The remaining 1% neutral hadron contamination consisted primarily of K_L^0's (Ref. 2); for this reason the neutral hadron component is referred to as the "K_L^0 component" below.

Figure 2 shows the shape of the beam energy spectrum. The shape was determined from measurements taken with a lead-glass block placed in the beam and is in excellent agreement with the results of other methods used by this experiment to measure the beam energy spectrum.[3] The total number of photons incident upon the target while the detector was "live" was determined in two independent ways: (1) using a quantameter which intercepted the noninteracting beam and (2) recording electron-positron pair production events under a heavily prescaled trigger. The "live" number of photons between 45 and 225 GeV was 1.12×10^{10} for the hydrogen running and 6.54×10^{10} for the deuterium running.

We give a brief description of the experimental apparatus important to the measurements reported here; further details on the target and the recoil detector are given in Ref. 4, while the rest of the apparatus is described in Ref. 1. The layout of the target and detector appears in Fig. 3. The target consisted of 40 cm of either liquid hydrogen or deuterium. Two concentric hexagonal

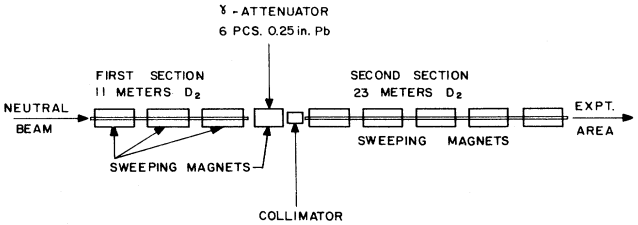

FIG. 1. The liquid-deuterium filter.

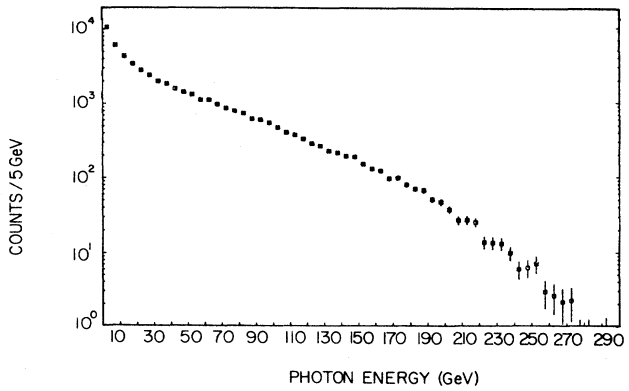

FIG. 2. Photon beam energy spectrum for 350-GeV/c primary protons.

rings of scintillator counters (RC) surrounding the target provided recoil detection. Momentum measurement for charged tracks was accomplished with a system of five multiwire proportional chambers ($P0$–$P4$) and two analyzing magnets ($M1$, $M2$) which bent particles in the vertical plane and had parallel ("defocusing" mode) momentum kicks of 0.523 GeV/c and 0.808 GeV/c. The scintillator counters $O\mu$, located just downstream of the $M2$ iron, and the set of crossed scintillator counters μH and μV served to detect muons. Two multicell Cherenkov counters ($C1$, $C2$) with π, K, p thresholds 5.9, 20.9, 39.7 GeV/c and 10.7, 37.8, 71.9 GeV/c provided charged hadron identification. Photons were detected using a fly's-eye arrangement of lead-glass (LG) blocks. Hadronic energy was measured by a steel-scintillator sandwich (HC) downstream of the lead-glass array. The vertical band of electron-positron pairs passing through the vertical gap in the lead-glass array was absorbed before the hadron calorimeter by a lead-scintillator sandwich (BS). (However, both the BS and HC detectors had holes in the center to allow the noninteracting beam to pass through.) The quantameter (Q) used for flux measurement was located just behind the hadron calorimeter.

In addition, the detector contained several sets of scintillator counters for triggering purposes. Forty-four small overlapping scintillator counters (T) immediately downstream of the target detected the production of charged particles. A set of crossed scintillator panels (HV) behind $P4$ detected charged particles outside the narrow vertical swath of copious e^+e^- production. Veto counters (A_μ, not shown in Fig. 3) upstream of the target flagged halo muons and charged particles in the beam. Scintillator counters (AW) mounted just outside the active region of $P1$ were used primarily to veto events with charged particles outside the acceptance of the multiwire proportional chambers (MWPC's).

[Also shown in Fig. 3, but not used by the analyses reported in this paper, are the outer electromagnetic (OE) calorimeter, the outer scintillator hodoscope (OH) for triggering on particles outside the aperture of $M2$, and the set of scintillator counters (CH) used in conjunction with $C2$ for flagging charged particles which did not leave light in $C2$.]

The data for the analyses reported below were taken under two triggers: one for the s and t dependence of ω and ϕ production from hydrogen and the other for heavy-particle production (including ϕ production) from deuterium. The hydrogen trigger required that (1) the A_μ counters be off; (2) at least one T counter be on; (3) there be hits in the HV counters consistent with two well-separated particles; (4) there be hits in the MWPC's consistent with two to five tracks traversing the length of the spectrometer; and (5) there be more than 20 GeV deposited in the hadrometer. The heavy-particle trigger for deuterium also had these requirements and in addition required that the sum of the $C2$ phototube outputs be less than four photoelectrons (eight photoelectrons were expected from $C2$ for a $\beta=1$ particle) and that no muons be detected.

The analyses rely upon special runs taken to understand backgrounds. Several runs were taken in which the photon component of the beam was effectively removed by inserting six radiation lengths of lead between the two sections of the liquid-deuterium filter (Fig. 1). The data taken during these runs are referred to as "K_L^0 data" below. Special runs were also taken with the target empty in order to measure the background due to coherent photoproduction from the Mylar end caps of the target.

III. ELASTIC ω PHOTOPRODUCTION

We have measured elastic photoproduction of ω vector mesons on hydrogen over the energy range $60 < E_\gamma < 225$ GeV. The ω was detected via its decay into $\pi^+\pi^-\pi^0$.

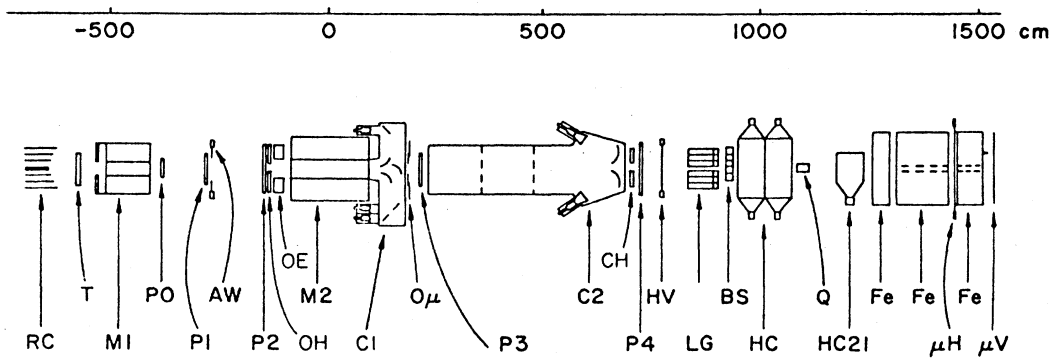

FIG. 3. Plane view of the E401 apparatus.

A. Event selection

Starting from the data acquired under the hydrogen trigger described in Sec. II, further cuts were applied to select the channel

$$\gamma p \to \omega p\ ,\quad \omega \to \pi^+\pi^-\pi^0\ ,\quad \pi^0 \to \gamma\gamma\ .$$

We required that exactly two oppositely charged tracks traverse the magnetic spectrometer and that they project to HV counters that were on. The point of closest approach between the tracks had to occur inside the target volume illuminated by the beam to within allowances made for the finite resolution of the vertex-finding algorithm. (The resolution was 7.5 cm in the beam direction and 0.05 cm in the nonbend view.) To further ensure only two charged particles in the forward-going state, the AW counters were required to be off.

A second set of cuts pertained to the hadron calorimeter. To reduce the number of events with shower leakage and thereby make the calorimeter performance easier to understand, the projection of each track to the calorimeter had to fall at least 12.5 cm inside the calorimeter boundary. The other cuts applied here are related to the method we used to correct for calorimeter bias in the trigger: In our results, events are weighted by the reciprocal of the efficiency of the calorimeter for triggering on an event. This efficiency is based on the hadronic energy reaching the calorimeter and a sum of the pulses from the HC phototubes. The hadronic energy, called $E_{\rm cal}$, is the difference between the total track energy $E_{\rm tot}$, as measured with the magnetic spectrometer, and the energy deposited by the tracks in the lead-glass (LG) array and the back shower (BS) counters. The sum of pulses from the HC phototubes, called $S_{\rm PAD}$, is the output of the pulse area digitizer which digitized the analog sum of the HC phototube dynode outputs and provided the energy signal for our triggers. Events with very small efficiencies, and thus large correction factors, were removed from the event sample by requiring that both $E_{\rm cal}$ and $S_{\rm PAD}$ be above a threshold (26.5 for both). The correction for removal of events due to the cuts on $E_{\rm cal}$ and $S_{\rm PAD}$ was made by additionally weighting each event in the final sample by the reciprocal of the fraction of events with total track energy $E_{\rm tot}$ which have $E_{\rm cal}$ and $S_{\rm PAD}$ above the threshold of 26.5. (The product of the two weights discussed above is called the "HC weight" below. The way in which the calorimeter efficiency was determined as a function of $E_{\rm cal}$ and $S_{\rm PAD}$ and the method we used to find the fraction of events passing the cuts on $E_{\rm cal}$ and $S_{\rm PAD}$ as a function of $E_{\rm tot}$ are described in Refs. 4 and 5.)

We required the number of π^0's reconstructed in an event to be only one. Reconstruction of π^0's was carried out in the following steps.[2] First, pulse heights in neighboring lead-glass blocks were associated into candidate electromagnetic showers. Second, the energy of each shower was calculated using the individual block calibration constants and the best position of the shower centroid was determined from the way in which the shower was shared among the blocks and geometrical factors. Third, we discarded showers with less than 1 GeV of energy and showers identified as having been left by tracks. Fourth, invariant masses were calculated for all possible pairings of the remaining showers and pairs having invariant mass which differed by more than 40 MeV/c^2 from the π^0 mass were dropped. (Figure 4 shows the invariant-mass spectrum for the case of two showers remaining after the cuts made in the third step.) Fifth, we refit the energies and centroids of the remaining shower pairs subject to the constraint that the refitted mass be the π^0 mass. We rejected shower pairs which to fit or for which the χ^2 yielded by the fit was greater than 10. Finally, the shower pairs surviving the cuts to this point were checked to see if two or more shared a common shower. If so, all pairs containing the common shower except the one with the lowest χ^2 were thrown out. We treated each shower pair left after this last step as a genuine π^0 with momentum calculated from the fitted shower quantities.

The signal in the recoil detector was required to be consistent with elastic production of the $\pi^+\pi^-\pi^0$ state. The recoil analysis[4] used the momenta of the downstream particles and the direction of the initial photon to predict the momentum of a recoil proton, assuming that the interaction was elastic. If the only scintillator counter hits in the recoil detector were consistent with the passage of the assumed recoil proton, allowing for multiple scattering and the uncertainty in the proton direction due to the resolution of the downstream tracks, the event was called elastic. An event was also called elastic if the proton could be expected to stop before hitting one of the recoil counters, and the recoil counters were off. Allowances were made for the straggling of the proton through the target, air, and scintillator, and for the uncertainty in the proton's momentum due to the uncertainties in the downstream track quantities. To reduce the effect of noise hits in the recoil detector, one or two unrelated counters were allowed to be on, provided they could not be associated with an extra particle coming from the target.

Lastly, we required that there be less than 4 GeV of energy in the lead-glass array unassociated with the tracks or the π^0. This cut not only eliminated events with addi-

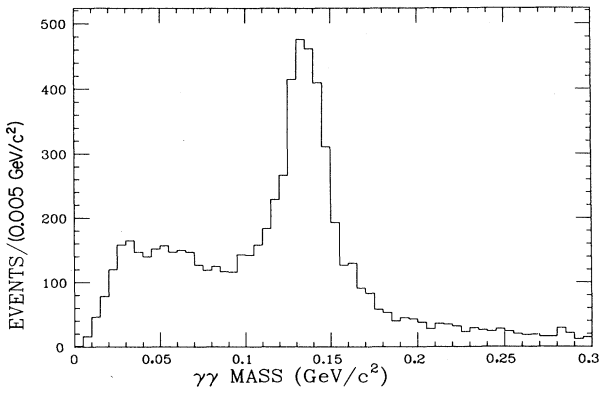

FIG. 4. Two-shower invariant-mass spectrum.

tional particles in the forward-going state but also provided a further bias against inelastic events.

Figure 5 shows the $\pi^+\pi^-\pi^0$ invariant-mass spectrum for events passing the above cuts in the range $60<E_\gamma<225$ GeV and $0<t<1$ $(\mathrm{GeV}/c)^2$. [The definition $t\equiv-(p_\gamma-p_V)^2$, where p_γ is the four-momentum of the beam photon and p_V is the total four-momentum of the $\pi^+\pi^-\pi^0$, K^+K^-, or $p\bar{p}$ final state, is used throughout this paper.] An ω peak containing about 300 events is clearly visible.

B. Backgrounds

Several significant backgrounds remain after applying the above event cuts. The first is ω production induced by the K_L^0 component of the beam. This background was removed by normalizing the K_L^0 data passing the above event cuts to the number of K_L^0's incident on target during the normal runs and subtracting the result bin by bin from the corresponding normal-data distribution. Figure 6 shows the $\pi^+\pi^-\pi^0$ mass distribution after the K_L^0 subtraction. (Negative differences are suppressed.) Based on a comparison of Figs. 5 and 6, about 6% of the ω signal and a much larger percentage of the background were K_L^0 induced.

The column headed "N_{fit}" in Table I gives the results of fitting for the number of ω's in the various kinematic regions after the K_L^0 subtraction. (θ is the polar angle of the normal to the decay plane in the ω helicity frame. The ω helicity frame is defined as the frame in which the ω is at rest and the z axis is antiparallel to the momentum vector of the recoiling proton.) The fits were made to the uncorrected mass distributions since the acceptance as a function of $\pi^+\pi^-\pi^0$ mass is practically flat across the range of the fit. The functional form used to fit the distributions was a Breit-Wigner line shape convoluted with a Gaussian, plus a noninterfering second-order polynomial background. The only parameter of the Gaussian-smeared Breit-Wigner function allowed to vary during the fit was the normalization; the experimental mass resolution ($\sim$15 MeV/c^2) and the center of the Breit-Wigner line shape were fixed by Monte Carlo simulation. A typical set of fits is shown in Fig. 7.

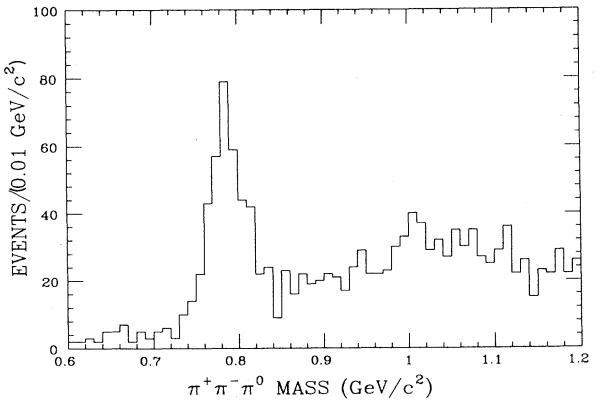

FIG. 5. $\pi^+\pi^-\pi^0$ mass spectrum for events passing the elastic ω cuts.

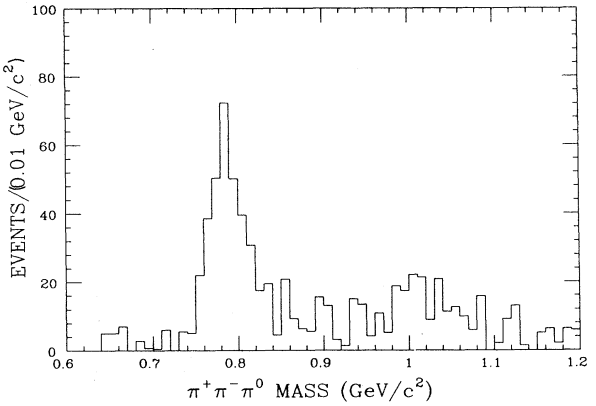

FIG. 6. $\pi^+\pi^-\pi^0$ mass spectrum after the K_L^0 subtraction.

A second source of background was photoproduction from the Mylar end caps of the target. To allow for the vertex resolution of 7.5 cm in the beam direction, we set the vertex cut to accept events with vertices between 14 cm upstream of the target and 14 cm downstream of the target. Consequently, most of the events produced from Mylar were also accepted.

As mentioned in Sec. II, several runs were taken with the target empty in order to measure the background from end-cap production. Too few ω's were detected during these runs, however, to determine a subtraction. The ρ signal in the empty-target data, on the other hand, was sizable, and we used that information as described below to determine the number of Mylar-produced ω's.

On the basis of measurements of ρ and ω photoproduction from complex nuclei at lower energies,[6] we assumed that the ρ and ω t spectra have the same shape for Mylar. This assumption, coupled with the fact that the acceptance as a function of t has approximately the same shape for the ρ as it does for the ω, allows us to take the shape of the uncorrected t spectrum for ω's produced on Mylar to be that of the uncorrected t spectrum for ρ's produced on the empty target.

To normalize the distribution we used information on production from the T counter during the normal and empty-target data runs. Let r_ρ be the ratio of the detected number of ρ's produced on the target end caps to the number of ρ's produced on the T counter during the empty-target runs. Let r_ω be the analagous ratio for ω production during the normal data runs. We assume $r_\omega=r_\rho$, good to within 10% according to Monte Carlo studies. Then, from measuring r_ρ in the empty-target data and counting the number of ω's produced from the T counter in the normal data runs, we find 19.3 ± 4.7 events due to production from Mylar. The distribution of Mylar-produced events in bins of t is given in Table I. Also given are the distributions of the Mylar-produced events in bins of energy and $\cos\theta$. For the latter distributions we assumed the number of Mylar-produced events N^j_{Mylar} in a particular bin j is given by

$$N^j_{\mathrm{Mylar}}=\left[N^j\Big/\sum_i N^i\right]N^T_{\mathrm{Mylar}}\ ,$$

where $N^T_{\mathrm{Mylar}}=19.3\pm4.7$ and N^j is the number of events

TABLE I. Signal and background distributions ($\gamma p \to \omega p$). The units of E are GeV and those of t are $(\text{GeV}/c)^2$.

Bin	N_{fit}	N_{Mylar}	$N^{\omega}_{\omega\pi^0}$	N_{subt}
$60 < E < 225$	282.0±22.5	19.3±4.7	46.1±16.5	216.6±28.3
$60 < E < 85$	86.7±13.3	6.1±1.7	18.3±6.4	62.3±14.9
$85 < E < 110$	94.2±13.5	6.6±1.7	14.9±5.2	72.7±14.6
$110 < E < 225$	95.0±13.5	6.6±1.7	11.2±3.9	77.2±14.2
$0 < t < 0.0214$	76.2±11.9	12.1±3.0	6.6±2.3	57.5±12.5
$0.0214 < t < 0.0477$	47.0±10.6	2.7±0.9	7.3±2.6	37.0±11.0
$0.0477 < t < 0.0815$	34.4±9.5	1.8±0.6	5.0±1.8	27.6±9.7
$0.0815 < t < 0.1450$	40.5±9.9	0.9±0.4	6.1±1.2	33.5±10.7
$0.1450 < t < 0.2923$	41.9±9.9	0.6±0.3	11.4±4.0	29.9±10.7
$0.2923 < t < 1$	31.4±9.0	0.6±0.3	11.5±4.3	19.3 ±10.0
$0 < \lvert\cos\theta\rvert < 0.25$	80.3±11.3	5.8±1.6	9.1±3.1	65.4±11.8
$0.25 < \lvert\cos\theta\rvert < 0.50$	70.6±12.2	4.9±1.3	13.8±4.7	51.9±11.8
$0.50 < \lvert\cos\theta\rvert < 0.75$	66.6±12.1	4.8±1.3	10.3±3.6	51.6±12.2
$0.75 < \lvert\cos\theta\rvert < 1$	51.9±11.9	3.8±1.2	14.1±1.2	34.0±12.9

(see column 1 of Table I) obtained in the fit to the K^0_L-subtracted data.

The third background we need to remove is due to $\omega\pi^0$ photoproduction: the cross section for $\omega\pi^0$ production is comparable to that of the ω and there is significant probability that the π^0 goes undetected while the ω passes the event cuts. Subtraction of the effects due to $\omega\pi^0$ production is handicapped by the fact that previous measurements[7] disagree on the production cross section and the dominant spin parity. However, since we are interested in $\omega\pi^0$ production only as a background here, a rough description is adequate.

We have obtained the approximate description of $\omega\pi^0$ production from the study of our own data.[8] We find that production occurs at an energy-independent cross section of 1.33 ± 0.43 μb and with events distributed in t according to $e^{-5.5t}$. The $\omega\pi^0$ mass distribution can be described by a Breit-Wigner function centered on 1.25 GeV/c^2 and having a natural width of 175 MeV/c^2. The limited data are consistent with s-channel helicity conservation (SCHC, described in Ref. 9) and a spin-parity assignment of 1^-.

The photoproduction of the $\omega\pi^0$ and our detector's response to it was studied using a Monte Carlo simulation. The simulated data were subjected to the ω analysis in order to determine the distribution of the $\omega\pi^0$ states

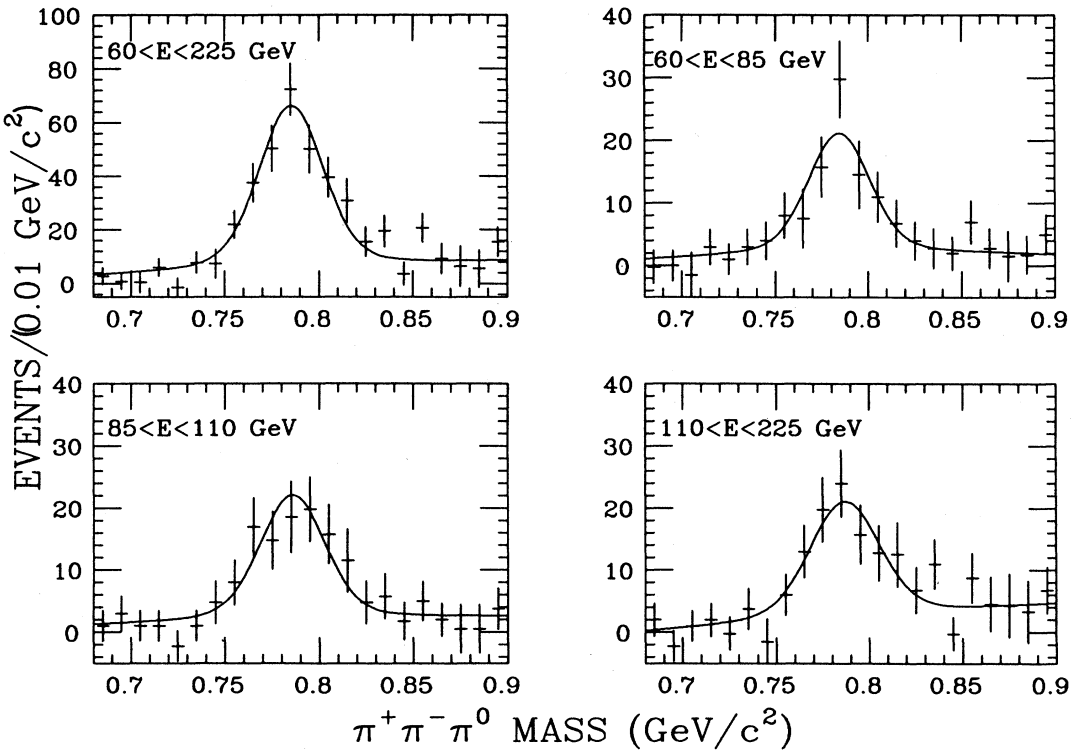

FIG. 7. $\pi^+\pi^-\pi^0$ mass spectra plus fits.

detected as elastically photoproduced ω's. These distributions were then normalized to $\omega\pi^0$ production in our experiment and are given in Table I.

We estimate the total number of $\omega\pi^0$ events passing the ω event cuts to be 46.1 ± 16.5. (This number is comparable to the number of $\omega\pi^0$ events we detect for photon energies greater than 60 GeV.) If we instead take the spin parity to be 1^+ with the S and D partial waves in the ratio $D/S=0.3$, then 51.5 ± 17.5 events in our ω sample are misidentified $\omega\pi^0$ events.

The last column in Table I gives the number of events after removal of the backgrounds discussed above. The uncertainties are obtained by adding in quadrature the uncertainties given in the preceding three columns.

C. Corrections

In converting the signal strengths given in the last column of Table I into cross sections, corrections have been made for (a) trigger bias; (b) geometrical acceptance; (c) track-reconstruction inefficiency; (d) π^0 reconstruction inefficiency; (e) event-selection bias; (f) electronic dead time; (g) target self-shielding; (h) absorption of charged pions; (i) π^0 photon conversion; and (j) branching ratio. With the exception of veto-counter accidental rates, trigger and event-selection bias due to the hadron calorimeter, and the effects of MWPC hit inefficiency on track reconstruction, corrections for (a)–(e) were determined from Monte Carlo data. (This included simulation of hadronic showers in the lead-glass array using data from elastic ρ photoproduction; for a description of the method, see Ref. 8.) The acceptances determined from simulation are given in the columns headed "Acceptance" in Tables II–IV. Determination of the correction for calorimeter bias, discussed above in Sec. III A, was carried out separately; the results are listed in the column headed $W_{\rm HC}$. Corrections (f) and (g) are automatically applied by using the electron-positron pair production data to calculate the effective flux $F_{\rm eff}$. The remaining correction factors are $f_{\rm abs}=1.07$ for charged-pion absorption, $f_{\rm MWPC}=1.06$ for MWPC inefficiency, $f_{\rm veto}=1.14$ for false vetos, $f_{\pi^0}=1.11$ for π^0 photon conversion, and $f_{\rm BR}=1/0.899$ for the branching ratio to $\pi^+\pi^-\pi^0$.

The measured event yields $N_{\rm subt}$ and the correction factors discussed above enter all cross-section calculations as the term

$$\frac{N_{\rm subt}W_{\rm HC}f_{\rm abs}f_{\rm MWPC}f_{\rm veto}f_{\pi^0}f_{\rm BR}}{F_{\rm eff}A\mathcal{A}},$$

where $A=1.715\times10^{-6}/\mu$b is the density of hydrogen atoms presented to the beam by the 40-cm-long target, and $\mathcal{A}$ is the acceptance.

The corrections give rise to systematic uncertainties in the cross-section normalization of $\pm10\%$ from π^0 detection, -5% from inelastic events misidentified as elastic, and $\pm5\%$ from photon-flux normalization. Checks of the shape of $d\sigma/dt$ have been carried out by varying the cuts which affect the shape of the t acceptance and the number of Mylar-produced events passing into the ω sample. These checks indicate a -10% systematic uncertainty in the exponential slope at small t.

D. Results and discussion

Table II gives the elastic cross sections $\sigma(\gamma p\to\omega p)$ averaged over bins in energy. (The uncertainties quoted are statistical and have been obtained by adding in quadrature the uncertainties in $N_{\rm subt}$ and "HC weight.") The hypothesis of a flat or rather mild energy dependence is in excellent agreement with our measurements, but due to large uncertainties the possibility of a significant dependence on energy cannot be ruled out.

We can use $\sigma(\gamma p\to\omega p)$ to determine $(\gamma_\omega^2/4\pi)$, where the inverse of γ_ω characterizes the strength of the photon-ω coupling in the vector-meson-dominance (VMD) model (Ref. 10). Combining VMD with the additive quark model (AQM) (Ref. 11), one obtains the prediction

$$\sigma(\gamma p\to\omega p)=(\alpha\pi/2\gamma_\omega^2)[\sigma(\pi^-p\to\pi^-p)+\sigma(\pi^+p\to\pi^+p)].$$

According to the results reported in Ref. 12, the $\sigma_{\pi p}$ cross sections are practically constant over the range $50<E<175$ GeV. Given the good agreement on energy dependence between our measurements and the AQM-VMD model, we may combine the above equation with our results to obtain $(\gamma_\omega^2/4\pi)$. Using

$$\sigma(\gamma p\to\omega p)=0.94\pm0.13\ \mu\text{b},$$

the cross section derived from fitting for the number of events in the full region $60<E_\gamma<225$ GeV, and

$$[\sigma(\pi^-p\to\pi^-p)+\sigma(\pi^+p\to\pi^+p)]/2=3.36\pm0.10\ \text{mb},$$

from Ref. 12, we get

$$(\gamma_\omega^2/4\pi)=6.5\pm0.9.$$

The differential cross sections $d\sigma/dt$, averaged over bins in t, are given in Table III for $60<E_\gamma<225$ GeV. The fractional errors are sizable, especially at larger values of t where the effects of the background subtraction due to $\omega\pi^0$ production are strongest. Nonetheless it is clear that the differential cross section clearly falls off rapidly with increasing momentum transfer.

Fitting the AQM-VMD prediction

TABLE II. $\sigma(\gamma p\to\omega p)$ as a function of energy.

Energy (GeV)	$N_{\rm subt}$	Acceptance	$W_{\rm HC}$	σ (μb)
60–85	62.3 ± 14.9	0.043	2.30 ± 0.26	0.91 ± 0.24
85–110	72.7 ± 14.6	0.057	1.63 ± 0.18	0.95 ± 0.22
110–225	77.2 ± 14.2	0.038	1.22 ± 0.11	0.94 ± 0.19

TABLE III. $(d\sigma/dt)(\gamma p \to \omega p)$ as a function of t.

t [(GeV/c)^2]	N_{subt}	Acceptance	W_{HC}	$\frac{d\sigma}{dt}$ [μb/(GeV/c)^2]
0–0.0214	57.5±12.5	0.051	1.69±0.10	10.41±2.35
0.0214–0.0477	37.0±11.0	0.045	1.69±0.10	6.23±1.89
0.0477–0.0815	27.6±9.7	0.035	1.69±0.10	4.64±1.65
0.0815–0.1450	33.5±10.7	0.043	1.69±0.10	2.43±0.79
0.1450–0.2923	29.9±10.7	0.047	1.69±0.10	0.87±0.32
0.2923–1	19.3±10.0	0.054	1.69±0.10	0.10±0.05

$$\frac{d\sigma}{dt}(\gamma p \to \omega p) = (\alpha\pi/4\gamma_\omega^2)\left[\left[\frac{d\sigma}{dt}(\pi^+ p \to \pi^+ p)\right]^{1/2} + \left[\frac{d\sigma}{dt}(\pi^- p \to \pi^- p)\right]^{1/2}\right]^2$$

to our results yields

$$(\gamma_\omega^2/4\pi) = 7.1 \pm 1.0$$

in good agreement with the determination based on $\sigma(\gamma p \to \omega p)$. (The parametrizations of the πp cross sections are taken from Ref. 12.) The cross sections with the fit superimposed are shown in Fig. 8. The t dependence predicted by AQM-VMD typically agrees with our results within uncertainties, but our measurements favor a somewhat faster falloff.

We have also fit a simple exponential form

$$\frac{d\sigma}{dt} = Ae^{-bt}$$

to the small momentum-transfer region $0 < t < 0.3$ (GeV/c)^2 and obtain

$$A = 10.7 \pm 2.2\ \mu\text{b/(GeV/}c)^2\ ,$$

$$b = 12.6 \pm 2.3/(\text{GeV/}c)^2\ .$$

The fit is shown in Fig. 9.

Finally, Table IV lists our measurements of $d\sigma/d|\cos\theta|$ averaged over bins in $|\cos\theta|$. (Recall θ is the polar angle of the normal to the decay plane in the ω helicity frame.) Production drops off as the decay plane becomes perpendicular to the ω direction of flight. Conservation of s-channel helicity requires

$$\frac{d\sigma}{d|\cos\theta|} \propto (1 - \cos^2\theta)\ .$$

Fitting a function proportional to $(1 - a\cos^2\theta)$ to our results gives

$$a = 0.90 \pm 0.17\ .$$

Within errors, s-channel helicity conservation is compatible with our results. Figure 10 shows the fit.

All measurements by various groups of elastic ω photoproduction from hydrogen at high energies indicate that the process is diffractive: the cross section varies little, if at all, with energy, the momentum-transfer distribution is sharply peaked toward zero, and the ω carries the same helicity as the photon. There are also differences between the various results, particularly with respect to the shape of the t distribution and the value of $(\gamma_\omega^2/4\pi)$. In the remainder of this section we review and discuss earlier photoproduction results together with our own and also compare photoproduction to e^+e^- annihilation with respect to $(\gamma_\omega^2/4\pi)$.

Table V compares our results for $\sigma(\gamma p \to \omega p)$ and $(\gamma_\omega^2/4\pi)$ with those of earlier experiments at high energy. Only results explicitly given by the references are listed.

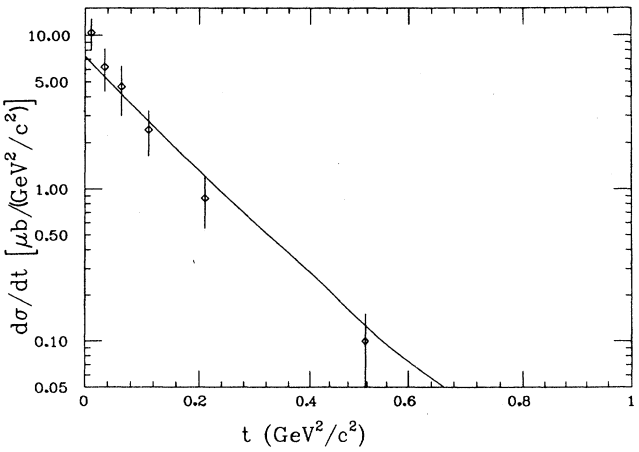

FIG. 8. $(d\sigma/dt)(\gamma p \to \omega p)$ vs t for $60 < E_\gamma < 225$ GeV. The smooth curve is the AQM-VMD fit described in the text.

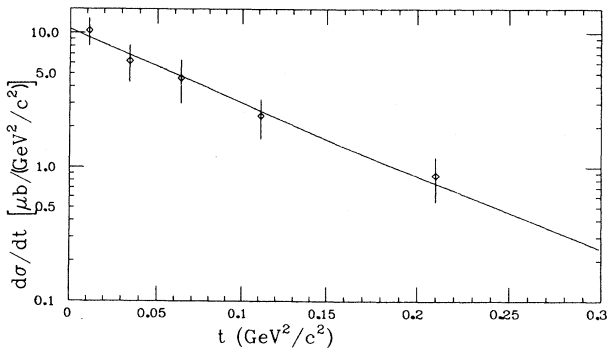

FIG. 9. $(d\sigma/dt)(\gamma p \to \omega p)$ vs t for small t fitted to the functional form Ae^{-bt}.

TABLE IV. $(d\sigma/d|\cos\theta|)(\gamma p \to \omega p)$ as a function of $|\cos\theta|$.

$\lvert\cos\theta\rvert$	N_{subt}	Acceptance	W_{HC}	$\frac{d\sigma}{d\lvert\cos\theta\rvert}$ (μb)
0–0.25	65.4±11.8	0.033	1.56±0.12	1.46±0.29
0.25–0.50	51.9±13.1	0.042	1.41±0.05	0.83±0.21
0.50–0.75	51.6±12.2	0.054	1.85±0.18	0.83±0.21
0.75–1	34.0±12.9	0.081	1.87±0.17	0.37±0.14

Systematic uncertainties, when given, are also listed. All values of $(\gamma_\omega^2/4\pi)$ were obtained using AQM-VMD. We also note the following details for the results given: Egloff *et al.*[13] obtained $(\gamma_\omega^2/4\pi)$ using the estimate that ρ-ω interference in the $\pi^0\gamma$ channel is a 20% effect. The cross section given by Breakstone *et al.*[14] was calculated ignoring ρ-ω interference, but the systematic uncertainty estimated for $(\gamma_\omega^2/4\pi)$ arises from ρ-ω interference. Also, Breakstone *et al.* did not make a measurement at $t<0.1$ $(\text{GeV}/c)^2$. To obtain the elastic cross section for ω photoproduction, they used AQM-VMD to extrapolate their measurements to low t.

Experiments observing ω photoproduction in the $\pi^+\pi^-\pi^0$ channel agree on $\sigma(\gamma p \to \omega p)$ to within statistical uncertainties. Comparison involving experiments that observe ω photoproduction in the $\pi^0\gamma$ channel is difficult because of ρ-ω interference. But since the determination of $(\gamma_\omega^2/4\pi)$ in the $\pi^+\pi^-\pi^0$ channel is not affected by interference, the results in that channel can be used to estimate the strength of interference effects in the $\pi^0\gamma$ decay mode. (We assume here that ω-ϕ interference and $\omega \leftrightarrow \phi$ transitions during scattering from hydrogen are small effects.) Before taking ρ-ω interference into account, Egloff *et al.* found $(\gamma_\omega^2/4\pi)=5.4\pm0.4$ and Breakstone *et al.* found 5.12 ± 0.35. For Atkinson *et al.*[15] we calculate $(\gamma_\omega^2/4\pi)=6.1\pm0.1\pm1.8$ corresponding to the cross section given in Table V. Uncertainties of one kind or another are large for each $\pi^+\pi^-\pi^0$ result but taken together and compared with the results of the experiments which detected the ω via its decay into $\pi^0\gamma$, they suggest ρ-ω interference in the $\pi^0\gamma$ channel is a 10% effect or stronger.

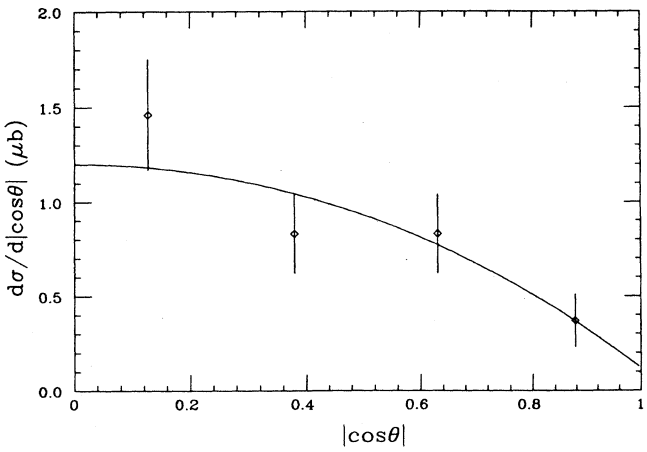

FIG. 10. $(d\sigma/d\cos\theta)(\gamma p \to \omega p)$ vs $\cos\theta$ for $60<E<225$ GeV. The smooth curve is a fit of form $A(1-a\cos^2\theta)$.

Table VI lists the slope parameters obtained by fitting e^{-bt} or e^{-bt+ct^2} to the $d\sigma/dt$ spectrum. Also given is the AQM-VMD prediction. Egloff *et al.* and Breakstone *et al.* used the AQM-VMD prediction to fit a function of form e^{-bt+ct^2} to $d\sigma/dt$ and found good agreement. As we have already noted, while the AQM-VMD prediction for the t dependence is consistent with our results, what we see favors a steeper t dependence.

Considering statistical uncertainties only, there is little agreement on the slope parameter b obtained by fitting e^{-bt} to the small-t region. Our result agrees only marginally with Egloff *et al.* and poorly with Atkinson *et al.* Further, Egloff *et al.* and Breakstone *et al.* do not agree very well with one another. Taking into account the systematic uncertainty of -10% in our measurement improves somewhat the agreement between our experiment and Egloff *et al.* Differences in the fitting regions and the AQM-VMD expectation that the slope parameter increases with E_γ may underlie the spread in results, but it seems unlikely they account entirely for it. Additional measurements of the t dependence of elastic ω photoproduction are clearly needed.

We last compare the measurement of $(\gamma_\omega^2/4\pi)$ in e^+e^- colliding-beam and photoproduction experiments. The most recent colliding-beam result, obtained taking ω-ϕ interference into account, is 5.1 ± 0.5 (Ref. 16). Neglecting systematic errors except those quoted for ρ-ω interference, results from high-energy photoproduction are 6.5 ± 0.5 (Engloff *et al.*), $5.12\pm0.35\pm0.50$ (Breakstone *et al.*), 6.1 ± 0.1 (calculated for Atkinson *et al.*), and 6.5 ± 0.9 from this experiment. Taken together, the photoproduction results favor a value of $(\gamma_\omega^2/4\pi)$ which is roughly 20% greater than the colliding beam value. This difference must, however, be viewed keeping in mind that the determination of $(\gamma_\omega^2/4\pi)$ from photoproduction assumes the validity of AQM, neglects $\omega \leftrightarrow \phi$ transitions, and either neglects or just roughly accounts for interference effects.

Let us elaborate on the last statement. In the absence of a measurement of $\sigma_{\omega p}$ at high energies from photoproduction on complex nuclei (see Ref. 17 for a review), AQM is the best way we have to estimate the ωp elastic cross section. There are, however, indications that AQM is not exact at high energies. For example, AQM predicts that

$$\pi^\pm p \to \rho X$$

and

$$\pi^\pm p \to \omega X$$

occur at the same rate. Observations are that the ω/ρ ra-

TABLE V. Experimental results on $\sigma(\gamma p \to \omega p)$ and $\gamma_\omega^2/4\pi$.

Experiment	Ref.	ω decay mode	Energy (GeV)	σ (μb)	$\gamma_\omega^2/4\pi$
Egloff *et al.*	13	$\pi^0\gamma$	46–180		6.5±0.5
Breakstone *et al.*	14	$\pi^0\gamma$	50–130	1.16±0.08	5.12±0.35±0.50
Atkinson *et al.*	15	$\pi^+\pi^-\pi^0$	20–70	1.01±0.015±0.290	
Experiment 401		$\pi^+\pi^-\pi^0$	60–225	0.94±0.13	6.5±0.9

tio is 0.90±0.15 (Ref. 18). Although consistent with AQM within errors, the best estimate of the ratio is 10% below the AQM prediction.

The photoproduction results have also been obtained assuming that vector-meson scattering is diagonal, i.e., that processes such as

$$\gamma \to \omega,\ \omega p \to \phi p\ ,$$

or

$$\gamma \to \phi,\ \phi p \to \omega p\ ,$$

do not occur. *A priori* there is no reason why off-diagonal transitions cannot occur, especially between the ω and ϕ (Ref. 19). It should also be noted that simple models which accommodate $\omega \leftrightarrow \phi$ mixing improve agreement between photoproduction measurements and VMD (Ref. 17).

In addition, there are interferences at work in ω photoproduction. Attempts have been made[13,14] to take into account ρ-ω interference in the $\pi^0\gamma$ channel, but the fact remains that the interference effects are rather uncertain. Interference between ω and ϕ photoproduction in the $\pi^+\pi^-\pi^0$ channel may be significant. Cordier *et al.*,[16] using models which incorporate ω-ϕ interference,[20] obtained a value of $(\gamma_\omega^2/4\pi)$ which is about 4% below the value one gets if interference is ignored.

It may also be that the coupling of the ω to the photon depends significantly on the photon mass. Given, however, that AQM may only be good to 10% and the uncertainty in mixing and interference, one cannot use current results from photoproduction to convincingly challenge the VMD claim that $(\gamma_\omega^2/4\pi)$ is independent of the mass at which the photon couples to the ω. We note that $(\gamma_\rho^2/4\pi)$, as determined from our experiment,[21] is also larger than that determined by colliding beam measurements, but by less than 10%. On the other hand, ϕ photoproduction leads to a $(\gamma_\phi^2/4\pi)$ which is almost a factor of 2 larger than the colliding beam value. Measurement of $(\gamma_\phi^2/4\pi)$ is discussed in more detail in the following section on ϕ photoproduction.

TABLE VI. Exponential slope parameters from $(d\sigma/dt)(\gamma p \to \omega p)$.

	t [(GeV/c)^2]	b [(GeV/c)$^{-2}$]	c [(GeV/c)$^{-4}$]
Egloff *et al.*	0.0–0.5	8.42±0.74	
Breakstone *et al.*	0.1–1.2	6.9±0.6	
Atkinson *et al.*	0.04–0.4	7.3±0.2	
	0.04–0.8	9.2±0.1	3.9±0.2
Experiment 401	0.0–0.3	12.6±2.3	
AQM-VMD		8.9	2.2

IV. ELASTIC ϕ PHOTOPRODUCTION

We measured elastic ϕ production on hydrogen and deuterium. The energy range of the hydrogen data is $35 < E_\gamma < 165$ GeV, while for the deuterium data it is $45 < E_\gamma < 85$ GeV. For both data sets, the invariant four-momentum-transfer squared t covers the range $0 < t < 1.0$ (GeV/c)^2. The ϕ was observed in its K^+K^- decay mode.

A. Event selection

Data for this measurement were taken under the main hadronic trigger for hydrogen and under the heavy-particle trigger for deuterium (described in Sec. II). Additional cuts on the data were imposed to attempt to ensure the exclusivity of the process $\gamma N \to \phi N$, where the ϕ decays to K^+K^-, and N refers to a proton, neutron, or deuteron.

We required two oppositely charged five-chamber tracks which extrapolated back to a vertex at the target. The z coordinate of the vertex had to be within 6.3 cm of the target volume, and the nonbend coordinate had to be within 0.5 cm of the beam edge. In the hydrogen data, the opening angle between the tracks in the nonbend plane had to exceed 0.5 mr. The z-vertex cut and the opening-angle cut reduced the number of the copiously produced e^+e^- pairs, which had essentially no opening angle and an apparent vertex at the center of magnet $M1$. Tracks were also required to project to inside the HV counters, and the counters thus hit had to satisfy the trigger requirements.

The following "diffractive" cuts required there be no evidence for other particles in the events: the AW counters had to be off; no π^0's could be found by the lead-glass analysis; no more than 5 GeV of energy not associated with a charged track could be present in the lead glass; and the information from the recoil counter was required to be consistent with an elastic event. In the hydrogen data, elastic events were defined as those in which the recoil counter showed evidence of a nucleon recoiling, or had no activity at all if, based on the information of the forward-going particles, it was likely that the recoil proton would not pass through the recoil counter. This definition was used previously in studying J/ψ photoproduction.[3] For deuterium, this definition was modified to allow for "elastic" production off neutrons, which do not generate any signals in the recoil counter. Thus, the lack of an expected recoil signal in the deuterium data was considered consistent with an elastic event.

Cuts were also made to reduce the energy bias imposed by the hadron calorimeter (HC). As described in Sec. III,

events were weighted by the reciprocal of the efficiency that the HC would accept the event. The weighting scheme for kaons was different from that for the pions in the ω analysis because of their different energy-deposition characteristics, especially in the lead glass. Tracks had to extrapolate to more than 12.5 cm inside the HC to reduce energy leakage and $S_{\rm PAD}$ both had to be greater that 25 GeV. In deuterium, they had to be greater than 45 GeV.

To reduce the number of nonkaons in the sample, we applied a loose Cherenkov requirement that removed few kaons by demanding that at least one particle of the pair have signals in both Cherenkov counters "consistent" with a kaon. This requirement meant that the observed signal had to be close to the most likely kaon signal within broad limits, which were chosen to exclude 2% of the largest and smallest of the expected kaon signals. A track below kaon threshold was labeled consistent with a kaon if a zero signal was observed, and labeled inconsistent with a kaon if a nonzero signal was observed. When signals were unavailable for a particular track (e.g., when light cones of two particles overlapped a single mirror), the track was also called consistent with a kaon.

In the deuterium data, no light was allowed to fall on the central four mirrors of $C2$, whose outputs were used in the heavy-particle trigger (as described in Sec. II). The phototubes for these mirrors were permanently and seriously degraded by the passage of many low-energy electrons through them. To remove their effect on the heavy-particle trigger, events whose particles would produce light on these mirrors were removed. Particles were assumed to be kaons when calculating their Cherenkov light distribution.

The mass plots of remaining events are displayed in Fig. 11 for the hydrogen data and in Fig. 12 for the deuterium data. Clear ϕ peaks are evident.

B. Background and corrections

We corrected our results for processes other than elastic ϕ photoproduction from the target.

Outside the ϕ peak, the background production processes are predominantly photon-induced low-mass $\pi\pi$ pairs [the low-mass tail of the ρ (Ref. 21)], and K_L^0-induced $K\pi$ pairs, as measured in our data. In fitting the hydrogen data for the number of ϕ's, the background on either side of and beneath the ϕ peak was completely fixed to be the sum of these two processes, the only free parameter being the number of ϕ's. Since the heavy-particle deuterium trigger had a much larger and cleaner signal, this process was not necessary, and we used a polynomial determined by the fit to approximate the background.

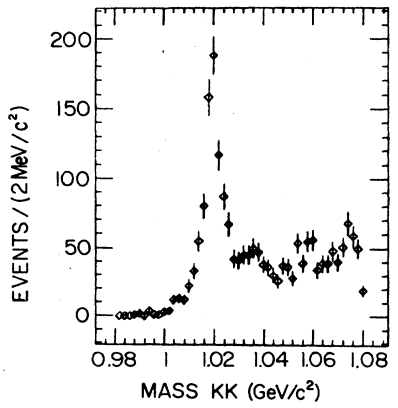

FIG. 11. ϕ sample from the hydrogen data.

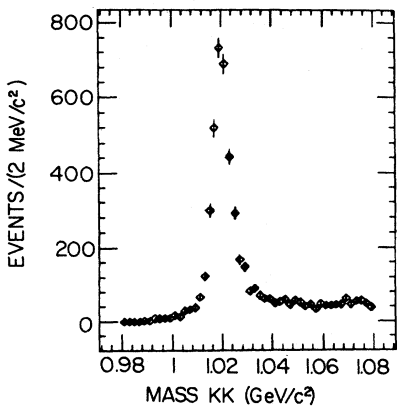

FIG. 12. ϕ sample from the deuterium data.

Correction for K_L^0 production of ϕ's was also made. In the hydrogen data, the correction was determined by fitting for the number of ϕ's in the K_L^0 data under the same cuts as the photon data. Since this correction was small ($\sim$4%) and the data were few, the correction was incorporated as an overall normalization factor. The deuterium data contained more events and so the K_L^0 correction ($\sim$10%) was able to be done bin by bin.

Two other corrections performed were t dependent. Inelastic production from the target, not detected by the recoil counter, was estimated at 8% for hydrogen and 17% for deuterium. Contributions from the target end caps were measured at 4.7% for hydrogen, and 1.9% for deuterium. (The procedure for this correction is described in Sec. III.)

Yields were also corrected for the following effects (hydrogen/deuterium): wire-chamber track-reconstruction inefficiency (5.9%/4.6%); A_μ/AW accidental veto rate, which is the fraction of time the A_μ or AW counters veto a legitimate event (12.6%/10.9%); K-decay probability (energy dependent, from 9.4% at 40 GeV to 2.5% at 140 GeV for the hydrogen data/from 15% at 45 GeV to 8% at 85 GeV for deuterium); spectrometer absorption (5.0%/8.3%). (The differences between the hydrogen and deuterium corrections for K decay are due to the inclusion of the Cherenkov counter $C2$ in the kaon decay volume for the deuterium measurement.) Scintillator-counter inefficiencies are included in the spectrometer acceptance calculation of the Monte Carlo simulation, and are generally less than 1%.

Events are weighted by the reciprocal of the product of the calorimeter efficiency and the fraction of events which survive the cuts on $E_{\rm cal}$ and $S_{\rm PAD}$; geometric acceptance is calculated by Monte Carlo simulation.

The systematic uncertainties differ for the hydrogen

and deuterium data sets. For the hydrogen data, there is a 4% uncertainty between the two methods of flux normalization and a 7% systematic uncertainty in the fitting procedure. These uncertainties combine to give an 8% systematic uncertainty, taken to be our experimental error. For the deuterium data, there is a 10% flux normalization uncertainty, as well as an 11% uncertainty in the Cherenkov trigger/identification algorithms. These combine to give our total systematic uncertainty of 15%.

C. Results and discussion

To measure the s and t dependence of ϕ photoproduction, the ϕ yield was determined in each energy and t bin by fitting for the number of ϕ's in the mass distribution. The mass resolution of the ϕ was fixed to be a convolution of the natural width and the experimental resolution, as determined from Monte Carlo calculations. Contributions from the two effects were comparable.

The results of both the hydrogen and deuterium measurements are presented in Fig. 13 for the s dependence and in Fig. 14 for the t dependence. Tables VII and VIII list our s-dependent cross sections for hydrogen and deuterium; Tables IX and X list the t-dependent measurements. Included in the tables are the yields, calorimeter weight, geometric acceptance, decay probability, and cross section. Errors in these tables are purely statistical.

Besides our hydrogen and deuterium measurements, Fig. 13 displays the previous measurements from the tagged photon experiment in this energy range.[22] While our hydrogen measurements agree well with theirs, our deuterium measurements appear ~20% lower than both their previous measurements and our own hydrogen results, assuming the cross section is proportional to the number of nucleons. From nuclear shadowing effects, one expects the deuterium cross section per nucleon to be about 5% lower than the hydrogen cross section.[23] The remaining discrepancy could be attributable to our systematic normalization uncertainties.

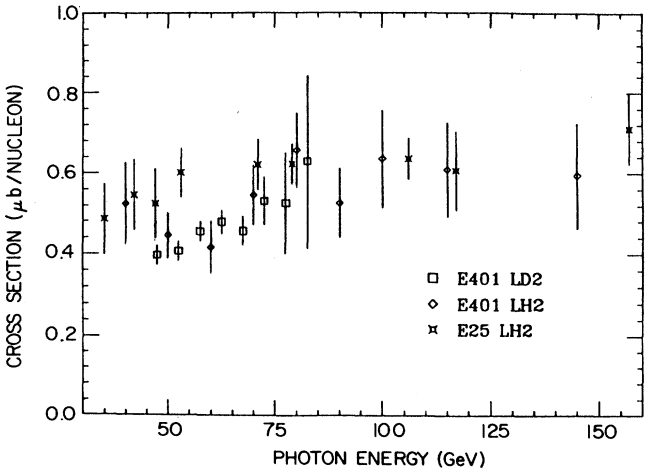

FIG. 13. The elastic ϕ cross sections as a function of energy for the hydrogen data, the deuterium data, and Fermilab Experiment No. E25 (Ref. 22).

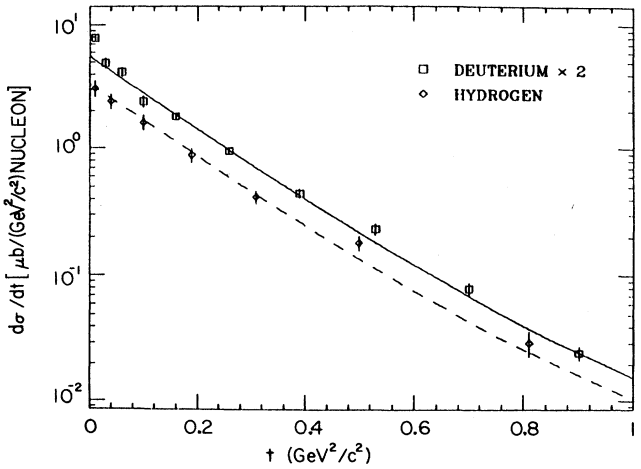

FIG. 14. $(d\sigma/dt)(\gamma N \to \phi N)$ for hydrogen and deuterium data. The dashed and solid lines are fits to the AQM-VMD model described in the text.

The ϕ cross section rises noticeably between 35 GeV and 165 GeV, as evidenced by our data and the previous experiment.[22] The deuterium measurements indicate that most of this rise occurs below 100 GeV. This rise in the cross section with energy is not as large as the rise in the cross section of the heavier J/ψ (Ref. 3), but contrasts with the nearly energy-independent cross sections of the lighter ρ (Ref. 21) or the ω (Sec. III).

The $d\sigma/dt$ distributions given in Fig. 14 are the first to be measured at this high energy, and show the sharply forward peaked cross-section characteristic of diffractive processes. A coherent peak is evident in the deuterium data for $t < 0.1$ $(\mathrm{GeV}/c)^2$. Both distributions flatten out at larger t values, which could be caused by an imperfect inelastic recoil correction. Estimating the yield from inelastic target processes is a difficult procedure, and the relative error becomes larger at higher t values, since elastic production itself becomes very small. Fitting the data to the form

$$\frac{d\sigma}{dt} = Ae^{-bt+ct^2} + A_{\mathrm{coh}}e^{-b_{\mathrm{coh}}t}$$

gives the results shown in Table XI.

Superimposed on Fig. 14 are fits using vector-meson dominance (VMD) and the additive quark model (AQM) referenced in Sec. III. The fits are of the form (via VMD)

$$\frac{d\sigma}{dt}(\gamma p \to \phi p) = (\pi\alpha/\gamma_\phi^2)\frac{d\sigma}{dt}(\phi p \to \phi p)$$

relating the "elastic" process of $\gamma p \to \phi p$ to the elastic process $\phi p \to \phi p$. In terms of AQM, the scattering $\phi p \to \phi p$ is related to the scattering of kaons and pions off protons by

TABLE VII. $\sigma(\gamma p \to \phi p)$ as a function of energy (hydrogen target).

Energy (GeV)	Events	Weight	Acceptance	Decay prob.	σ (μb/nucleon)
35–45	68.4±8.2	2.63±0.40	0.1781	0.916	0.524±0.101
45–55	148±14	1.80±0.15	0.3775	0.932	0.446±0.56
55–65	127±12	1.54±0.18	0.3587	0.943	0.417±0.063
65–75	119±12	1.46±0.13	0.2985	0.951	0.545±0.074
75–85	117±12	1.26±0.12	0.2572	0.957	0.656±0.093
85–95	73.7±9.6	1.12±0.10	0.2188	0.962	0.526±0.084
95–105	55.5±7.5	1.14±0.12	0.1709	0.966	0.635±0.120
105–125	55±8.7	1.14±0.12	0.1237	0.970	0.608±0.116
125–165	38.5±7.21	1.03±0.12	0.0768	0.976	0.594±0.131

$$\frac{d\sigma}{dt}(\phi p \to \phi p) = (1/P_\phi^{*2}) \left\{ P_K^* \left[\left[\frac{d\sigma}{dt}(K^+ p \to K^+ p) \right]^{1/2} + \left[\frac{d\sigma}{dt}(K^- p \to K^- p) \right]^{1/2} \right] - P_\pi^* \left[\frac{d\sigma}{dt}(\pi^- p \to \pi^- p) \right]^{1/2} \right\}^2 ,$$

where P_ϕ^*, P_K^*, and P_π^* are the momenta of the elastically scattering particles in the center of mass, and where the only free parameter is $(\gamma_\phi^2/4\pi)$. The separate hadronic elastic scattering cross sections were measured by a previous elastic scattering experiment.[12] To remove the effect of the coherent slope in deuterium, the region $t < 0.1$ $(\mathrm{GeV}/c)^2$ was excluded from the deuterium fit. Agreement between the model prediction and the data is excellent, illustrating the validity the VMD-AQM picture of scattering. From the hydrogen data we get a value for $(\gamma_\phi^2/4\pi)$ of 5.93±0.30, while for the deuterium data we obtain a value of 6.70±0.23.

Integrating these differential cross sections at different energies allows a determination of the energy-dependent cross sections. Fitting the energy-dependent cross sections for $(\gamma_\phi^2/4\pi)$ gives the fits displayed in Fig. 15, and yields values for $(\gamma_\phi^2/4\pi)$ of 5.68±0.30 for hydrogen, and 6.55±0.18 for deuterium. These values are in good agreement with the determination from $d\sigma/dt$. Approximately half of the 10% discrepancy between hydrogen and deuterium may be due to nuclear shadowing effects. The remainder may arise from our normalization uncertainties.

Both values of $(\gamma_\phi^2/4\pi)$, however, are in marked disagreement with the value obtained from e^+e^- colliding-beam experiments, where the value of $(\gamma_\phi^2/4\pi)$ is measured as 3.30±0.15 (Ref. 24). This disagreement has been noted previously, and indicates a factor of 2 weaker coupling of the photon to the ϕ in photoproduction than in e^+e^- annihilation. For the case of the ρ and ω, however, the difference between photoproduction and e^+e^- annihilation with respect to the photon-meson coupling is much less: the couplings agree to within 10% for the ρ (Ref. 21) and differ by not much more than 20% for the ω.

There are two main theoretical speculations why photoproduction and e^+e^- production are so different in their photon-ϕ couplings: an interference between the ϕ and the ω, and a difference in the coupling for the ϕ between real and virtual photons. In the first case, the ϕ and ω photoproduction cross sections are believed to interfere destructively, possibly with transitions between one another, resulting in a lower effective coupling constant between the ϕ and the photon.[25,26] In the second case, differences between real and virtual photons may allow the coupling between a real photon and a ϕ to be weaker than the coupling between a virtual photon and a ϕ (Ref. 27). More detailed experimental measurements of ϕ and ω production phases may help clarify this situation.

V. PHOTOPRODUCTION OF HIGH-MASS K^+K^- PAIRS

We investigated the exclusive production on deuterium of possible high-mass states decaying into K^+K^- pairs.

TABLE VIII. $\sigma(\gamma N \to \phi N)$ as a function of energy (deuterium target).

Energy (GeV)	Events	Weight	Acceptance	Decay prob.	σ (μb/nucleon)
45–50	566±29	2.09±0.07	0.2899	0.857	0.397±0.025
50–55	621±31	1.84±0.06	0.2995	0.870	0.406±0.023
55–60	637±26	1.68±0.05	0.2742	0.881	0.455±0.023
60–65	529±27	1.56±0.06	0.2150	0.890	0.478±0.031
65–70	367±24	1.45±0.06	0.1645	0.897	0.457±0.036
70–75	179±16	1.38±0.09	0.072	0.904	0.530±0.059
75–80	37±7.5	1.33±0.16	0.0160	0.910	0.525±0.124
80–85	20±5.6	1.22±0.24	0.0074	0.915	0.629±0.214

TABLE IX. $(d\sigma/dt)(\gamma p \to \phi p)$ as a function of t (hydrogen target). ϵ_{MT} is the fraction of production from the empty target. ϵ_{NL} is the fraction of production due to inelastic processes.

t [(GeV/c)^2]	Events	Weight	Acceptance	MT $(1-\epsilon_{MT})^{-1}$	Inelastic $(1-\epsilon_{NL})^{-1}$	$\frac{d\sigma}{dt}$ [μb/(GeV/c)^{2}nucleon]
0.00–0.02	109±13	1.60±0.14	0.2839	1.143	1.040	3.07±0.46
0.02–0.06	111±13	1.44±0.11	0.1760	1.050	1.074	2.39±0.32
0.06–0.14	131±11	1.62±0.18	0.1698	1.023	1.121	1.60±0.23
0.14–0.24	156±13	1.48±0.14	0.2768	1.023	1.126	0.88±0.11
0.24–0.38	148±13	1.24±0.10	0.3330	1.023	1.131	0.41±0.05
0.38–0.62	122±11	1.34±0.13	0.3860	1.023	1.160	0.18±0.02
0.62–1.00	40.7±6.6	1.32±0.20	0.4166	1.023	1.363	0.03±0.006

There have been few other published observations of high-mass dikaon production.[28–31] We find evidence for such a state at 1.72 GeV/c^2, consistent with a previous report.[30]

A. Event selection

Events taken under the heavy-particle trigger from deuterium were subjected to the same cuts as for the ϕ, as discussed in Sec. IV. Stricter Cherenkov requirements were imposed to reduce the background of unwanted particles. Each track had to leave signals in both Cherenkov counters "consistent" with those of a kaon, i.e., in a wide region around the most likely signal expected from a kaon, chosen to exclude the smallest and largest 2% of kaon signals. In addition, each track had to leave a signal in at least one Cherenkov counter that was much smaller than the signal expected to be left by a pion of the same momentum. The cut was made to exclude the largest 90% of signals expected from pions. Similarly, protons were removed by demanding that at least one track leave a signal much greater than that expected from a proton. This cut excluded the smallest 98% of the signals expected from protons. The K^+K^- mass distribution of the remaining events is given in Fig. 16, along with events from the K_L^0 data.

The two most evident characteristics of the mass spectrum are its overall decrease with increasing K^+K^- mass, and a broad structure between 1.5 GeV/c^2 and 1.8 GeV/c^2. A similar structure is also seen in the K_L^0 data. Part of this rise, discussed more fully in the next section, is caused by misidentifying the decay products of the $K^*(1430)$, a kaon and a pion, as two kaons, and including such events in the K^+K^- mass plot.

B. Backgrounds

The most significant background to this high-mass K^+K^- investigation is production from the K_L^0 component of the initial beam. Understanding our background is essential to this measurement.

Figure 17 shows the mass distribution of $K\pi$ events taken from the K_L^0 data. The energy and fiducial cuts are the same used for the ϕ (Sec. IV), while the Cherenkov requirements define a $K\pi$ event. Signals from the kaon and pion tracks had to be within a wide range of their most likely values, which excluded only the largest and smallest 2% of their expected respective signals. In addition, the kaon track had to leave a signal in at least one of the Cherenkov counters that was much smaller than the signal expected from a pion. This requirement removed the highest 90% of the signals expected from pions. The pion track had to leave a signal in at least one Cherenkov counter that was greater than the signal expected from most of the kaons; specifically, this cut removed the lowest 80% of signals expected by kaons. Two resonances expected from an initial K_L^0 beam are evident: the $K^*(890)$ and the $K^*(1430)$.

TABLE X. $(d\sigma/dt)(\gamma N \to \phi N)$ as a function of t (deuterium target). ϵ_{MT} is the fraction of production from the empty target. ϵ_{NL} is the fraction of production due to inelastic processes.

t [(GeV/c)^2]	Events	Weight	Acceptance	MT $(1-\epsilon_{MT})^{-1}$	Inelastic $(1-\epsilon_{NL})^{-1}$	$\frac{d\sigma}{dt}$ [μb/(GeV/c)^{2}nucleon]
0.00–0.02	367±21	1.74±0.07	0.1551	1.048	1.029	3.91±0.27
0.02–0.04	181±14	1.78±0.10	0.1243	1.023	1.058	2.46±0.24
0.04–0.08	278±18	1.73±0.08	0.1058	1.011	1.107	2.08±0.16
0.08–0.12	215±19	1.76±0.93	0.1381	1.009	1.166	1.19±0.12
0.12–0.20	510±28	1.73±0.07	0.2177	1.010	1.142	0.92±0.06
0.20–0.32	540±27	1.74±0.07	0.2841	1.011	1.176	0.47±0.03
0.32–0.46	366±25	1.67±0.10	0.3222	1.011	1.270	0.21±0.02
0.46–0.60	209±17	1.70±0.10	0.3078	1.011	1.449	0.11±0.01
0.60–0.80	169±16	1.67±0.10	0.3906	1.011	1.842	0.040±0.004
0.80–1.00	91±11	1.55±0.13	0.3385	1.011	3.501	0.012±0.002

TABLE XI. Parameters from fit to $d\sigma/dt$ from elastic ϕ production.

	Deuterium	Hydrogen
A_{coh}	4.98 ± 8.6 $\mu b/(GeV/c)^2$	0 (fixed)
b_{coh}	31.9 ± 9.3 $(GeV/c)^{-2}$	0 (fixed)
A	4.16 ± 0.34 $\mu b/(GeV/c)^2$	3.11 ± 0.33 $\mu b/(GeV/c)^2$
b	5.66 ± 0.28 $(GeV/c)^{-2}$	6.8 ± 0.8 $(GeV/c)^{-2}$
c	-0.10 ± 0.28 $(GeV/c)^{-4}$	1.2 ± 1.1 $(GeV/c)^{-4}$

When the invariant mass of these events (requiring good $K\pi$ identification) is calculated by (incorrectly) assigning the kaon mass to both particles, the K^+K^- mass distribution in Fig. 18 results. The shoulder in the K^+K^- mass distribution around 1.5 GeV/c^2 to 1.65 GeV/c^2, from the miscalculated mass of the $K^*(1430)$, is responsible for the rise in the K^+K^- mass distribution of the K_L^0 data in Fig. 16.

To better understand the shape of the misidentified $K^*(1430)$ in a K^+K^- mass plot, we weight each accepted $K\pi$ event in Figs. 17 and 18 by the relative probability that the event would satisfy the Cherenkov requirements imposed on K^+K^- events, described in Sec. V A. The resultant weighted K^+K^- mass spectrum is plotted in Fig. 19. Also plotted in Fig. 19 is the K^+K^- mass spectrum of events from the K_L^0 data satisfying the diffractive cuts and the K^+K^- Cherenkov requirements. The normalization between these distributions is arbitrary, however, since demanding good $K\pi$ identification eliminates events that are not replaced by the weighting scheme; nor have the diffractive cuts been applied to the weighted events. Nevertheless, by the compelling similarity of the shapes of the distributions between 1.5 GeV/c^2 and 1.65 GeV/c^2, we conclude that the structure at this mass in the K_L^0 data is a misidentified $K^*(1430)$.

Figure 20 shows the K^+K^- spectrum after subtracting the background of the K_L^0-induced events. The K_L^0 subtraction is performed using the empirical fit to the K_L^0 mass distribution shown in Fig. 16, and the ratio of the intensities of the photon and K_L^0 data (2.292). Performing a bin-by-bin subtraction does not significantly change these results. Two structures are now visible, one around 1.2 GeV/c^2 and the other around 1.7 GeV/c^2.

The structure at 1.2 GeV/c^2 is the reflection of the ρ decaying into two pions, where both pions are misidentified as kaons. The dotted line in Fig. 20 represents the amount of contamination expected from $\pi\pi$ events, based on the number of ρ's observed in the $\pi\pi$ mass spectrum (127 ± 54) using the same Cherenkov and diffractive cuts. The Monte Carlo prediction of 89 ± 35 ρ events, based on the number of ρ's observed when just the consistent kaon requirements are enforced (1115 ± 65 ρ's), is entirely consistent with the observed number. (An *a priori* prediction of the number of ρ's in these distributions, using the flux and ρ section, is not as accurate because the absolute ρ acceptance is much less than 1%.) This agreement is indicative of the performance of the Cherenkov algorithm.

The remaining events in Fig. 20 are more than 90% K^+K^-, as estimated for the mass region between 1.5 GeV/c^2 and 1.8 GeV/c^2. Applying various Cherenkov

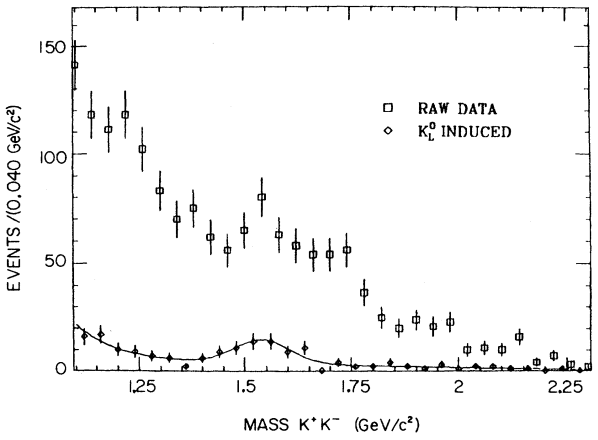

FIG. 16. K^+K^- mass spectrum for photon and K_L^0-induced events. The exposure of the photon data corresponds to 2.92 times the exposure for the K_L^0-induced events.

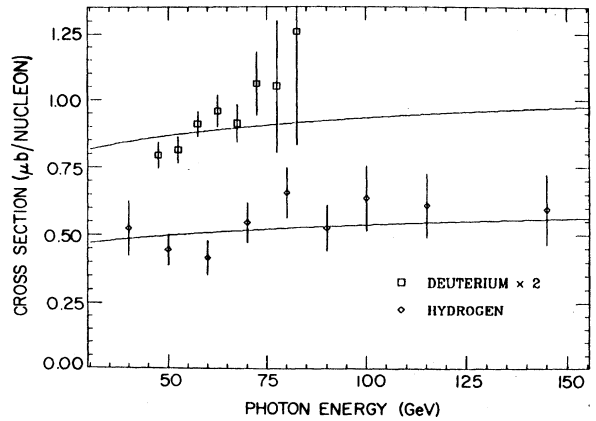

FIG. 15. The elastic cross section $\sigma(\gamma N\rightarrow\phi N)$ as a function of energy. The solid lines are fits to the AQM-VMD model described in the text.

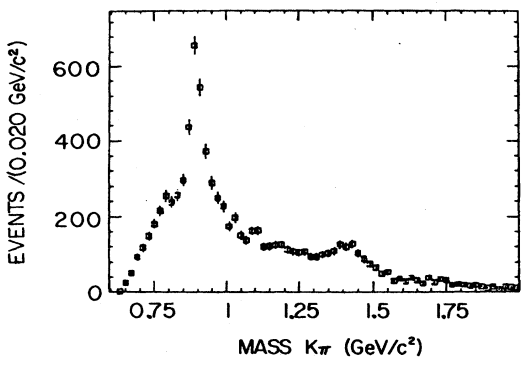

FIG. 17. $K\pi$ mass distribution of K_L^0-induced events, requiring good $K\pi$ Cherenkov identification. $K^*(890)$ and $K^*(1430)$ peaks are evident.

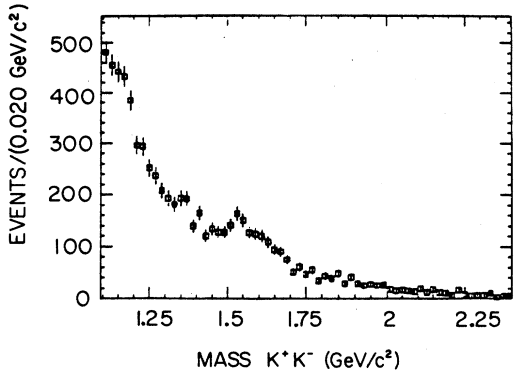

FIG. 18. K^+K^- mass distribution of K_L^0-induced events. Events chosen have good $K\pi$ Cherenkov identification, but the pion is assumed to have the mass of the kaon.

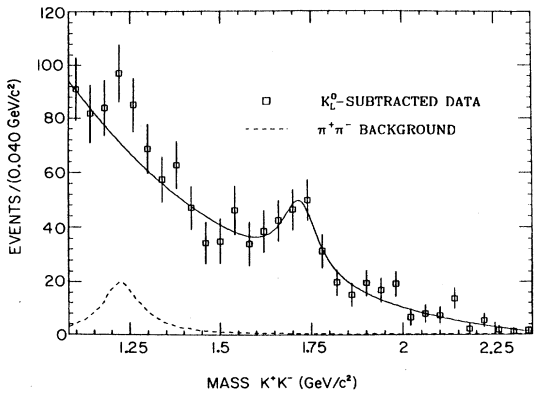

FIG. 20. K^+K^- mass distribution after subtracting K_L^0-induced component. Dotted line shows contamination from misidentified $\pi^+\pi^-$ events, including $\rho\to\pi^+\pi^-$.

cuts to the events in this region, and assuming that the events are either K^+K^-, $\pi\pi$, or $p\bar{p}$, and that the Monte Carlo simulation accurately predicts the relative acceptances of these types of events under these Cherenkov cuts, allows us to estimate the relative amounts of K^+K^-, $\pi\pi$, or $p\bar{p}$ in this plot. This procedure indicates that approximately 91–96% of the events in this region are K^+K^-.

C. Analysis and results

Fitting the mass distribution of Fig. 20 with a Breit-Wigner distribution to describe the enhancement, and an exponential+linear term to describe the background, yields the parameters

$$\text{mass}=1.726\pm0.022\ \text{GeV}/c^2\ ,$$

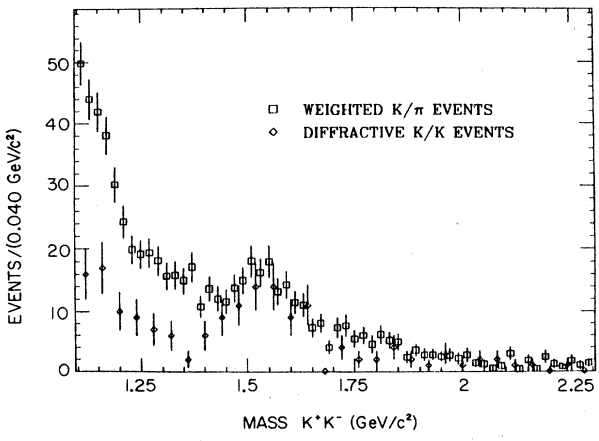

FIG. 19. K_L^0-induced events, showing (a) (diamonds) K^+K^- mass distribution, requiring good K^+K^- Cherenkov identification, and using the usual diffractive cuts, (b) (squares) K^+K^- mass distribution where (i) the events chosen have good $K\pi$ Cherenkov identification but the pion is assumed to have the mass of the kaon and (ii) each event is weighted by the probability it would be accepted by good K^+K^- Cherenkov identification. The normalization between the two distributions is arbitrary.

$$\text{FWHM}=0.121\pm0.047\ \text{GeV}/c^2\ ,$$

$$\text{number of events}=123\pm41\ .$$

Since the experimental resolution at this mass is $\sim$8–9 MeV/c^2, the Breit-Wigner form of the resonance is the natural way to describe it. The fit shown in Fig. 20 has a χ^2 probability of 45%, while a fit excluding the Breit-Wigner term yields a probability of 1.5%. This probability puts the significance of this enhancement close to the 3σ level.

We calculate a cross section×branching ratio σ_B for this state using the corrections for chamber efficiency, accidental veto counter rate, kaon decay, spectrometer absorption, scintillator inefficiency, target end-cap production, inelastic production, and hadronic trigger energy bias as described in Sec. IV C for the ϕ. Geometric acceptance is calculated based on the assumptions of s-channel helicity conservation (SCHC, which gives a $\sin^2\Theta_H$ distribution, where Θ_H is the angle, in the K^+K^- center-of-mass frame, between the K^+ and the direction of the recoiling nucleon), and a $d\sigma/dt$ distribution proportional to $e^{-4.7t}$, as measured for events with $1.5<M_{K^+K^-}<1.8$ GeV/c^2. Changing the assumed Θ_H distribution to be flat in $\cos\Theta_H$ would increase the cross section by $\sim$30%, while changing the $d\sigma/dt$ distribution to either $e^{-3.7t}$ or $e^{-5.7t}$ would change the cross section by less than 1%.

The total σ_B is $8.0\pm2.7\pm1.4$ nb. The first uncertainty is purely statistical. The second uncertainty is the systematic error of this measurement, from uncertainties in normalization (10%), Cherenkov triggering/identification uncertainty (11%), and the inclusion of the inelastic correction (9%). Although we do not have evidence of inelastic production, because the $d\sigma/dt$ distribution is shown to be consistent with that of the ϕ, we use the same fraction for inelastic contamination. These effects yield the total systematic uncertainty of 17%.

Although the statistics are poor, we make the first attempt to measure production characteristics of this state. In each energy region, the mass distribution is fit for the number of events in this enhancement, with the mass and

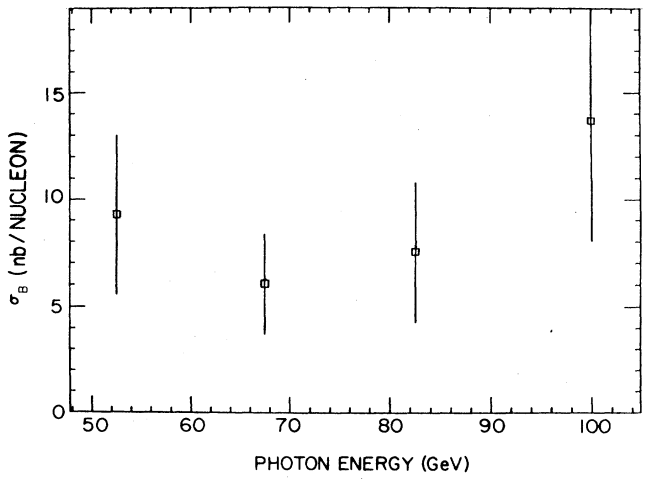

FIG. 21. The product of $\sigma(\gamma N \to K^+K^- N)$ and the K^+K^- branching ratio for the enhancement in the K^+K^- mass spectrum at 1.72 GeV/c^2.

width fixed to the values above. The cross section in four energy regions is shown in Fig. 21. Although it is consistent with being flat, we cannot rule out, at the 90% confidence level, a rise as much as a factor of 2.6 from 50 GeV to 100 GeV.

We also attempt to measure the t dependence of the differential cross section, $d\sigma/dt$. Fitting for the yield in different regions of t gives the distribution plotted in Fig. 22. A fit to the form e^{-bt} gives $b=6.1\pm2.2/(\text{GeV}/c)^2$ for $0.08<t<0.60$ $(\text{GeV}/c)^2$; for $0.0<t<1.0$ $(\text{GeV}/c)^2$, $b=6.2\pm1.3/(\text{GeV}/c)^2$. Simply fitting the t distribution for events with $1.64<M_{K^+K^-}<1.80$ GeV/c^2 yields $b=5.0\pm0.8/(\text{GeV}/c)^2$. Since background events are included in this second sample, it is not surprising that the slope is not as steep as in the previous technique. The t distribution of the background, defined as $1.3<M_{K^+K^-}<1.52$ GeV/c^2, or $M_{K^+K^-}>2.0$ GeV/c^2, yields a slope $b=3.3\pm0.7/(\text{GeV}/c)^2$. These results point to the fact that this enhancement at 1.72 GeV/c^2 is produced with a t dependence steeper than that of the background, although conceivably consistent with it.

A simple spherical harmonic moment analysis indicates that the enhancement is consistent with a spin-1 particle. The enhancement is evident in Fig. 23, which shows the K^+K^- mass distribution obtained by weighting each event by the negative of the spherical harmonic $Y_2^0(\Theta_H)$. On this plot no K_L^0 subtraction has been performed, and some of the K_L^0 background around 1.5 GeV/c^2 is also visible. The 1.72-GeV/c^2 enhancement is not seen in the $Y_4^0(\Theta_H)$ moment of the K^+K^- distribution, as can be seen in Fig. 24. Although this behavior is consistent with a spin-1 object,[32] it is not conclusive evidence because we do not have complete angular acceptance.

Assuming that all K^+K^- pairs come from the decay of a 1^- particle obeying SCHC, and produced with a $d\sigma/dt$ distribution proportional to $e^{-4.7t}$, we calculate the cross section for the K^+K^- mass spectrum displayed in Fig. 25. Superimposed on this plot is the acceptance curve under these assumptions. The acceptance is a fairly smooth function, without abrupt variations that could cause artificial enhancements.

D. Discussion

Our investigation of high-mass photoproduced K^+K^- pairs ($M_{K^+K^-}>M_\phi$) shows the presence of an object with a mass of 1.726 ± 0.022 GeV/c^2, a width of 0.121 ± 0.047 GeV/c^2, and a σ_B of 8.0 ± 2.7 nb, with an additional systematic uncertainty of 1.4 nb. Very little can be said about the energy dependence, as it is consistent with being flat, or rising a factor of more than 2 between 50 and 100 GeV. The t dependence of this state, assumed to be exponential, has a slope of

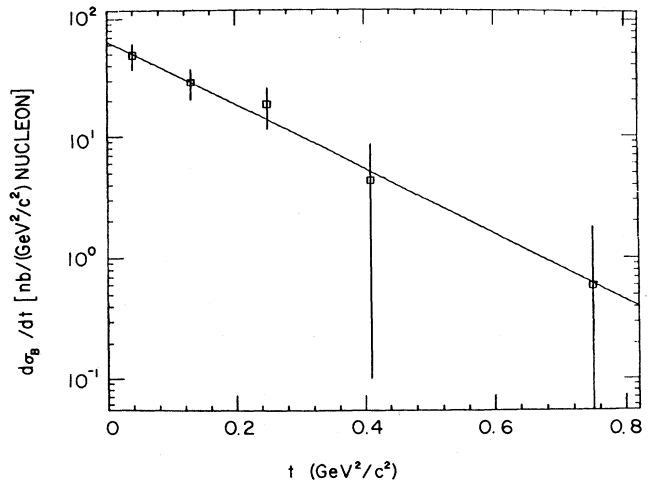

FIG. 22. The product of $(d\sigma/dt)(\gamma N \to K^+K^- N)$ and K^+K^- branching ratio for the enhancement in the K^+K^- mass spectrum at 1.72 GeV/c^2. The line is an exponential of the form Ae^{-bt} with $b=6.2/(\text{GeV}/c)^2$.

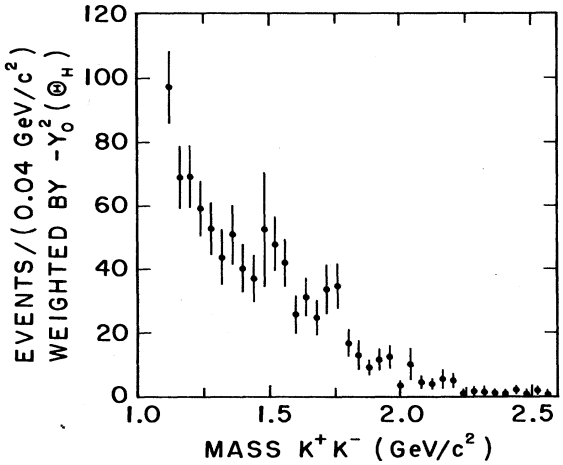

FIG. 23. The K^+K^- mass spectrum where each event is weighted by the $-Y_0^2(\Theta_H)$. The angle Θ_H is the polar angle of the K^+ in the helicity frame of the K^+K^- system. The contribution from K_L^0-induced events has not been subtracted.

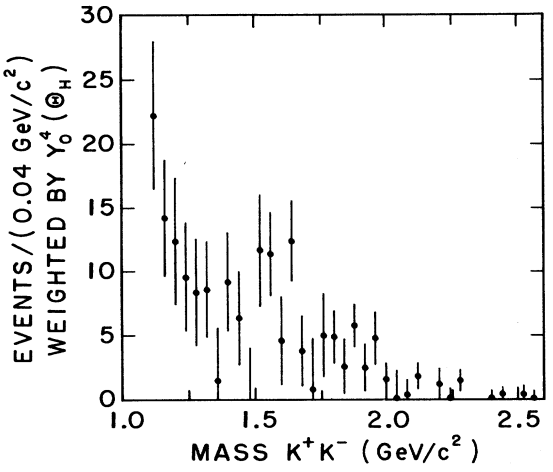

FIG. 24. Same as Fig. 23 except each event is weighted by the $Y_0^4(\Theta_H)$.

$6.2\pm1.3/(\mathrm{GeV}/c)^2$, found to be steeper than that of the background, but quite similar to that of the ϕ's. Although not conclusive, a partial sum of the spherical harmonic moments indicates that the enhancement is consistent with spin 1.

One can draw the conclusion that the object we have observed is a ϕ', a radial excitation of the ϕ. One previous photoproduction experiment has already reported a very similar state, with a mass of 1.748 ± 0.011 GeV/c^2, a width of 0.080 ± 0.033 GeV/c^2, and a σ_B of 8 ± 3 nb (Ref. 30). Our results are completely consistent with theirs. This enhancement was also reported in an earlier version of this experiment with a mass of 1.75 and a width of 0.131 GeV/c^2 (Ref. 31), and in one other experiment with a mass of 1.75 GeV/c^2 (Ref. 28).

In several e^+e^- colliding beam experiments, reports have been made of a state called ϕ' which decays into K^+K^-, K^*K^0, $K_L^0K_S^0$, and $\omega\pi\pi$.[33–36] The mass distributions of the different decay channels in the e^+e^- experiments are very different, which is attributed to interference effects from other particles in the region of the ϕ' (Ref. 37). However, the mass reported in these experiments

$$\text{mass}=1.68\ \mathrm{GeV}/c^2\ ,$$

$$\Gamma=0.185\pm0.022\ \mathrm{GeV}/c^2$$

is lower than that in all the photoproduction experiments. The previous experiment with similar results as ours was able to attribute their observations to a ϕ' with a mass of 1.68 GeV/c^2 (Ref. 30). A similar discrepancy is seen in the ρ, which, because of interference from competing channels, has different apparent masses in e^+e^- production and in photoproduction.

Another comparison with the ρ-ρ' system may be made. An investigation into the photoproduced ρ' and its t-dependent production characteristics has shown that the ρ' is produced with a t dependence much steeper than its background.[38] We have shown here that the t dependence of the enhancement at 1.73 GeV/c^2 is steeper than its background, and is very similar to the ϕ's. This similarity to the ρ-ρ' system also suggests the identification of the state at 1.73 GeV/c^2 as a ϕ'.

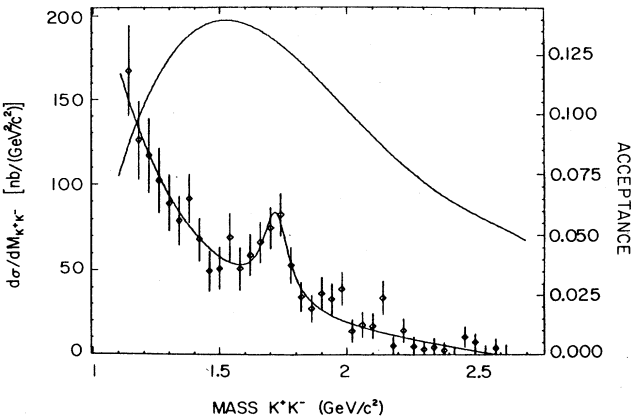

FIG. 25. $(d\sigma/dM_{KK})(\gamma N\to K^+K^-N)$ under assumptions stated in the text. The solid acceptance curve on top uses the scale on the right.

VI. ELASTIC AND INELASTIC $p\bar{p}$ PHOTOPRODUCTION

In "elastic" $p\bar{p}$ photoproduction we measure $d\sigma/dM_{p\bar{p}}$, and investigate our data for previously reported $p\bar{p}$ states, especially from electroproduction. No such states are observed. In "inelastic" $p\bar{p}$ photoproduction we examine our data for evidence of a $p\bar{p}$ state reported in conjunction with other particles.[39] We do not find such evidence.

A. Elastic $p\bar{p}$ photoproduction

1. Event selection

Events were recorded under the same trigger as the K^+K^- data from deuterium. The same geometric, diffractive, and energy cuts were applied as for the high-mass K^+K^- analysis described in Sec. V A. Light cones of the particles were now assumed to be generated by protons instead of kaons for the requirement that no light fall on the four central mirrors of $C2$.

Cherenkov requirements for obtaining a clean $p\bar{p}$ sample were that each track leave signals in both Cherenkov counters close to the most likely signal expected from a proton, removing only the highest and lowest 2% of signals expected from protons; that each track leave a signal in at least one Cherenkov counter that was smaller than most of the pions, removing the greatest 95% of the signals expected from pions; and that at least one track leave a signal in a Cherenkov counter that was smaller than most of the signals expected from kaons, thus excluding the greatest 95% of the signals expected from kaons.

The mass distribution of the surviving events is given in Fig. 26, along with the events from the K_L^0 data. There are no obvious peaks or resonances in this distribution.

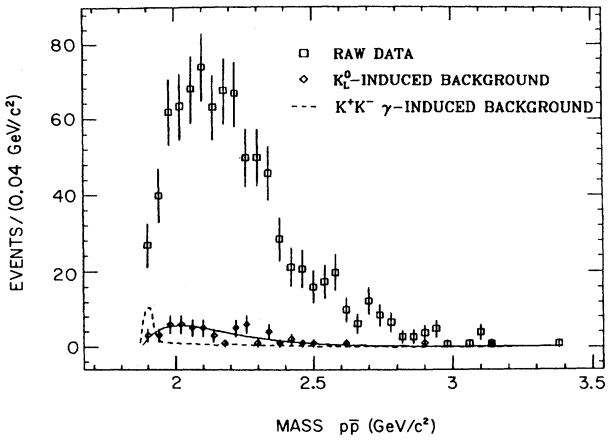

FIG. 26. $p\bar{p}$ mass spectrum for photon and K_L^0 data. The exposure of the photon data is 2.92 times the exposure for the K_L^0-induced data. Also shown by the dotted line is the expected contamination from misidentified K^+K^- events, including $\phi \to K^+K^-$.

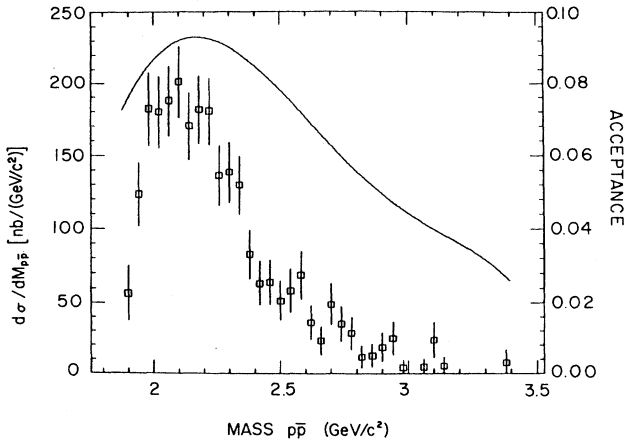

FIG. 27. $(d\sigma/dM_{pp})(\gamma N \to p\bar{p}N)$ under assumptions stated in the text. The solid acceptance curve uses the scale on the right.

2. *Backgrounds*

The fraction of K_L^0-produced events is much smaller here than in the K^+K^- investigation, since the initial beam has a strange-particle contamination which produces kaons more frequently than proton-antiproton pairs. Photon-induced K^+K^- events are also a small background, as shown in Fig. 26. This distribution is normalized to the number of ϕ's seen in the K^+K^- mass distribution under the same selection criteria (10 ± 5). Photon-induced $\pi\pi$ events contribute little to this sample: 0 ± 80 ρ events are found in the $\pi\pi$ mass distribution of these events.

We estimate the percentage of $p\bar{p}$ events in this sample to be between 94% and 99%, in a way analogous to the previous estimate of K^+K^- purity in Sec. V B. The present estimate uses the events with $2.0 < M_{p\bar{p}} < 2.5$ GeV/c^2, their behavior under various Cherenkov cuts, the assumption that these events consist only of $\pi\pi$, K^+K^-, and $p\bar{p}$, and the relative acceptances of these type of events predicted by the Monte Carlo data. Contributions from πK, πp, and Kp are ignored. The cleanliness of this $\sim$95%-pure $p\bar{p}$ sample is consistent with the small measured K^+K^- and $\pi\pi$ contaminations.

One object we might expect to see in this channel is the J/ψ. Assuming a production cross section of 25 ± 5 nb/nucleon,[3] a branching ratio for $J/\psi \to p\bar{p}$ of $0.22\%\pm0.02\%$ (Ref. 40), and the acceptance of the Monte Carlo data, we expect to see 0.75 ± 0.25 events. Extrapolations of the $p\bar{p}$ mass distribution to this region, 3.08 GeV/$c^2 < M_{p\bar{p}} < 3.12$ GeV/c^2, predict 1.4 ± 0.5 events, yielding a total of 2.1 ± 0.6 events expected in this mass region: we see 4 events.

3. *Results and discussion*

To convert the yield into a cross section, corrections are made for chamber efficiency, accidental veto rate, target end-cap production, energy bias, and counter efficiency, as described in previous sections. Spectrometer absorption for $p\bar{p}$ pairs is taken to be 18.4%. For calculating the geometric acceptance, the following assumptions are made: that the $p\bar{p}$ pairs are the decay products of a spin-1 object obeying SCHC, resulting in a $(1+\cos^2\Theta_H)/2$ helicity angle distribution; and, that this object is produced with an exponential t dependence having a slope of 3.7. We further assume that 17% of the observed elastic production arises from misidentified inelastic events (the same fraction found for the ϕ). The resulting $d\sigma/dM_{p\bar{p}}$ distribution is given in Fig. 27, along with the acceptance for these events.

Assuming an exponential t dependence and fitting the t distribution between $t=0.08$ (GeV/c)^2 and $t=0.6$ (GeV/c)^2 gives a slope of 3.7/(GeV/c)^2. The t distribution becomes flatter at higher masses. This effect is not unreasonable, if $p\bar{p}$ production occurs through a Drell-Soding process.[41]

There are no immediately apparent peaks or resonances in this channel. Production rises up quickly from threshold, reaches a broad plateau, and then decreases more slowly. The data may show some structure above 2.5 GeV/c^2, reminiscent of the K^+K^- mass spectrum, but we have found no evidence of any enhancements in this region.

It is unlikely that this structure is due to misidentifying the kaons from the enhancement at 1.72 GeV/c^2 as protons. The estimated contamination of this sample by non-$p\bar{p}$ events is small, as witnessed by the small measured K^+K^- contribution from ϕ decay. Also, if the kaons from the enhancement at 1.72 GeV/c^2 were misidentified as a $p\bar{p}$ pair, their mass would be less than 2.45 GeV/c^2. Therefore, the K^+K^- spectrum is not responsible for this shoulder.

One possible sign of a resonance or enhancement is a sharper t distribution, as measured for the enhancement at 1.72 GeV/c^2 in the K^+K^- spectrum. However, the t distribution of the $p\bar{p}$ events shows a flattening of the t distribution as the mass increases. Above 2.5 GeV/c^2,

the t distribution has an exponential distribution of about $e^{-0.8t}$, compared with a distribution of $e^{-3.7t}$ for the whole $p\bar{p}$ data.

Several states have been reported in the $p\bar{p}$ decay channel by electroproduction and other means, but not by photoproduction.[42–47] While we do not see any evidence for these states, we set limits on their production from photons. From the mass distribution in Fig. 26 we can calculate the confidence levels that specific numbers of events coming from the decay of these states are present in our data. We assume that the states may be represented by Breit-Wigner distributions, that the number of events in these states follow a Gaussian distribution, and that the background may be represented by a polynomial. The cross section is calculated as for the $d\sigma/dM_{p\bar{p}}$ distribution in Fig. 27.

We thus establish limits at the 90% confidence level for the "elastic" production of these particles by photons (i.e., given our distribution of events, there is a 10% chance that the true cross section is more than the limit reported here). These limits are given in Table XII.

The disagreement between our limits and electroproduction results deserves some comment. Photoproduction and electroproduction both proceed via photons, the former using real photons, with the latter using virtual photons. However, the dependence of electroproduction cross sections on Q^2, the square of the four-vector difference between the incoming and outgoing electron momenta, is well understood and can be used to extrapolate to real photons. Hence, there is an apparent conflict between these two results. Given the poor statistical significance of the electroproduction results and the large errors attached to their measurements, it is reasonable to interpret their results as fluctuations. An earlier low-energy photoproduction experiment, having far fewer events than we, set a limit on the narrow state at 2.02 GeV/c^2 of 2 nb (Ref. 43), which we have much improved.

The results for the states observed in other processes may not be quite as applicable to the experiments of $\pi^- d$, $p\bar{p}$, and $\bar{p}d$, as to electroproduction. We simply cannot supply any evidence for their existence.

B. Inelastic $p\bar{p}$ photoproduction

1. Event selection and background

For this investigation we required at least some indication of inelasticity in an event: the presence of a π^0, more than 5.0 GeV of neutral energy, AW counters that were "on," or an inelastic recoil. The Cherenkov cuts on the tracks were the same as for the elastic $p\bar{p}$ case. The mass spectrum of the resulting events is given in Fig. 28, along with the events from the K_L^0 data satisfying the same requirements. As expected, the K_L^0 background is larger than in the elastic case.

2. Analysis

There are no immediately apparent resonances in the mass spectrum. One bin at 1.945 GeV/c^2 is about 2σ higher than the expected background. In 30 bins, the probability of getting at least one 2σ fluctuation is $\sim$75%. Without benefit of any further evidence, one must regard this excess as a statistical fluctuation.

The Omega spectrometer has reported a state at 1.930 ± 0.003 GeV/c^2, with a width of 9 ± 3 MeV/c^2, and a cross section of 5 ± 2 nb (Ref. 39). With our mass resolution of 3 MeV/c^2 at this mass, we cannot identify our high bin with their enhancement. Nor can our mass scale be shifted to make an object with a mass of 1.930 GeV/c^2 appear to have a mass of 1.945 GeV/c^2. If this were the case, we would observe other well-known particles at masses higher than the accepted values, which are the values we actually observe (e.g., we would see the ϕ at 1.028 GeV/c^2, instead of at 1.020 GeV/c^2, which is its correct mass). Thus, we cannot corroborate their report.

Given the reported cross section, we can calculate how many events we should expect to see. Reference 39 reports the cross section is flat over the range $x_F=0.6$ to $x_F=0.8$, where $x_F=P_\parallel^*/P_{\max}^*$, $P_{\max}^*$ is the maximum momentum a particle can have in the center-of-mass frame, and $P_\parallel^*$ is the momentum of the particle in the center-of-mass frame, parallel to the incoming particle. Extrapolating to the limits of our acceptance ($x_F=0.2$) gives a cross section of 12 ± 5 nb. Given this cross section we calculate the number of events we expect to see to be 104 ± 43, based on the Monte Carlo acceptance, photon spectrum, and calorimeter weight of events in the same mass region. We see 20 or fewer events at the 90% confidence level. For our results to be consistent we must veto $77\%\pm10\%$ of these events. To be more precise requires knowledge about the momentum distribution and the number of other particles.

C. Conclusion

Our investigation of the "elastic" process $\gamma d \rightarrow p\bar{p}(d/n/p)$ has produced a fairly clean sample of $p\bar{p}$ events. We have measured $d\sigma/dM_{p\bar{p}}$ assuming a $(1+\cos^2\Theta_H)/2$ helicity-angle distribution. No evidence

TABLE XII. Limits on $p\bar{p}$ production of previously reported states.

Mass (GeV/c^2)	Width (GeV/c^2)	Where seen	$\sigma(\gamma V)$ (nb)	Limit (nb)
1.93	0.12	$p\bar{p}$, $\bar{p}d$, γp (inelastic) (Refs. 39, 44, 45, and 46)		0.5
2.02	0.024	e^-p, π^-p (Refs. 42 and 47)	6.6 ± 2.2	0.77
2.20	0.016	π^-p (Ref. 47)		0.72
2.20	0.060	e^-p (Ref. 42)	5.0 ± 2.5	3.0

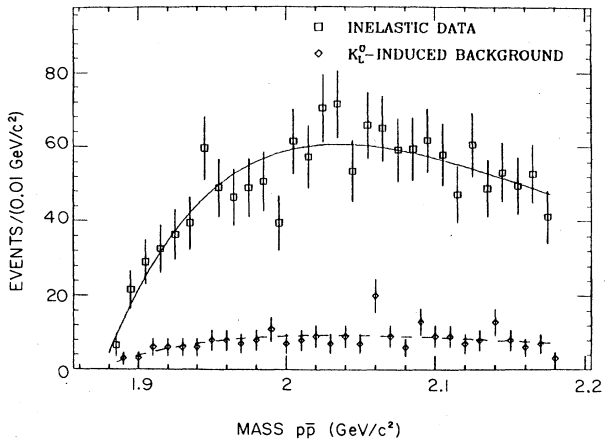

FIG. 28. $p\bar{p}$ mass distribution for inelastic photon and K_L^0 data. The exposure for the photon data is 2.92 times the exposure for the K_L^0-induced data.

of any enhancement is observed. Strict limits have been set on the production of previously reported possible $p\bar{p}$ states. In particular, the comparison of our results to two electroproduction experiments indicate that their observations were quite likely fluctuations.

Our investigation of the "inelastic" process $\gamma d \to p\bar{p}X$, where X stands for additional particles, does not support evidence for any enhancement in this channel. For our results to be consistent with a previous inelastic $p\bar{p}$ photoproduction cross section reported by the Omega spectrometer,[39] we must veto approximately $(77\pm10)\%$ of the expected 104 ± 43 events. A 2σ deviation at a mass of 1.945 GeV/c^2 cannot be associated with their report.

VII. SUMMARY

We have studied high-energy photoproduction of $\pi^+\pi^-\pi^0$, K^+K^-, and $p\bar{p}$ states. Having detected the ω via its decay into $\pi^+\pi^-\pi^0$, we observe elastic ω photoproduction between 60 and 225 GeV to have the following characteristics: (1) The cross section is consistent with being independent of energy and has a value of 0.94 ± 0.13 μb; (2) the differential cross section $d\sigma/dt$ falls off quickly with increasing t; fitting a function proportional to $\exp(-bt)$ to the region $t<0.3$ (GeV/c)^2 yields an exponential slope of 12.6 ± 2.3/(GeV/c)^2 with a -10% systematic uncertainty; and (3) the ω carries the same helicity as the photon.

We have measured the elastic ϕ photoproduction on both hydrogen and deuterium targets. Between 35 and 165 GeV the cross section rises by approximately 50%, reaching about 0.6 μb/nucleon at 165 GeV. The high-statistics deuterium measurement indicates that most of the increase occurs below 100 GeV. With the exception of $t<0.1$ (GeV/c)^2, where ϕ photoproduction from deuterium receives a contribution from coherent nuclear scattering, the measurement of $d\sigma/dt$ per nucleon yields qualitatively very similar results for hydrogen and deuterium. Quantitatively, the single-nucleon exponential slope is found to be 6.8 ± 0.8/(GeV/c)^2 for scattering from hydrogen and 5.66 ± 0.28/(GeV/c)^2 for scattering from deuterium. The slightly flatter slope observed in the deuterium data may be due to inelastic contamination.

We have also observed the photoproduction of a high-mass state decaying into K^+K^-. It has a mass of 1.726 ± 0.022 GeV/c^2 and a FWHM of 0.121 ± 0.047 GeV/c^2, and the product of the integrated cross section and branching ratio is 8.0 ± 2.7 nb. Production is consistent with being flat between 50 and 100 GeV, but our limited statistics cannot rule out a significant rise over the same interval. The t dependence is similar to that of the ϕ. The likely identification of this enhancement is ϕ'.

Finally, we have searched the $p\bar{p}$ channel for resonance production on deuterium. No enhancements, either elastically or inelastically produced, are observed, and we have set upper limits on the photoproduction of states reported from previous experiments.

ACKNOWLEDGMENTS

We would like to thank the staffs of Fermilab and the high-energy group of the University of Illinois for their support and cooperation. We also would like to thank the Nevis Laboratory for making available to us those parts of the spectrometer which they constructed as well as for the loan of the lead-glass array and Cornell University for the use of a 30D40 analyzing magnet. This research was supported in part by the U.S. Department of Energy.

*Present address: University of Notre Dame, Notre Dame, IN 46556.
†Present address: Bell Laboratories, Holmdel, NJ 07733.
‡Present address: Bell Laboratories, Holmdel, NJ 07748.
§Present address: University of Colorado, Boulder, CO 80309.
**Present address: Science Applications International Corporation, Bellvue, WA 98005.

[1]M. C. Goodman *et al.*, Phys. Rev. D **22**, 537 (1980).
[2]M. Lamm, Ph.D. thesis, University of Illinois, 1983.
[3]M. Binkley *et al.*, Phys. Rev. Lett. **48**, 73 (1982).
[4]P. Callahan, Ph.D. thesis, University of Illinois, 1983.
[5]C. Olszewski, Ph.D. thesis, University of Illinois, 1985.
[6]H.-J. Behrend *et al.*, Phys. Rev. Lett. **24**, 1246 (1970).
[7]R. Anderson *et al.*, Phys. Rev. D **1**, 27 (1970); J. Ballam *et al.*, Nucl. Phys. **B76**, (1984); D. P. Barber *et al.*, Z. Phys. C **4**, 169 (1980); D. Aston *et al.*, Phys. Lett. **92B**, 211 (1980); M. Atkinson *et al.*, Nucl. Phys. **B243**, 1 (1984).
[8]J. Busenitz, Ph.D. thesis, University of Illinois, 1985.
[9]F. J. Gilman *et al.*, Phys. Lett. **31B**, 387 (1970).
[10]J. J. Sakurai, Ann. Phys. (N.Y.) **11**, 1 (1960).
[11]H. J. Lipkin, Phys. Rev. Lett. **16**, 1015 (1966).
[12]D. S. Ayres *et al.*, Phys. Rev. D **15**, 3105 (1977).
[13]R. M. Egloff *et al.*, Phys. Rev. Lett. **43**, 1545 (1979); **44**, 690(E) (1980).
[14]A. M. Breakstone *et al.*, Phys. Rev. Lett. **47**, 1782 (1981).
[15]M. Atkinson *et al.*, Nucl. Phys. **B231**, 15 (1984).

[16]A. Cordier *et al.*, Nucl. Phys. **B172**, 13 (1980).
[17]M. T. H. Bauer *et al.*, Rev. Mod. Phys. **50**, 261 (1978).
[18]H. Kirk *et al.*, Nucl. Phys. **B128**, 397 (1977).
[19]M. Ross and L. Stodolsky, Phys. Rev. Lett. **16**, 563 (1966).
[20]F. M. Renard, Nucl. Phys. **B82**, 1 (1974).
[21]G. Gladding *et al.*, University of Illinois report, 1984 (unpublished).
[22]R. M. Egloff *et al.*, Phys. Rev. Lett. **43**, 657 (1979).
[23]V. Franco and R. G. Glauber, Phys. Rev. **142**, 1195 (1966).
[24]G. Cosme *et al.*, Phys. Lett. **63B**, 352 (1976).
[25]M. Ross and L. Stodolsky, Phys. Rev. **149**, 1172 (1966).
[26]G. Benaksas *et al.*, Phys. Lett. **39B**, 289 (1972).
[27]R. Aviv *et al.*, Phys. Rev. D **12**, 2862 (1975).
[28]F. Richard, in *Proceedings of the 1979 International Symposium on Lepton and Photon Interactions at High Energies,* Batavia, edited by T.B.W. Kirk and H.D.I. Abarbanel (Fermilab, Batavia, Illinois, 1980).
[29]D. Peterson *et al.*, Phys. Rev. D **18**, 3955 (1978).
[30]D. Aston *et al.*, Phys. Lett. **104B**, 231 (1981).
[31]W. Wisniewski, Ph.D. thesis, Columbia University, 1982.
[32]W. Koch, in *Analysis of Scattering and Decay,* edited by M. Nikolic (Gordon and Breach, New York, 1968).
[33]B. Delcourt *et al.*, Phys. Lett. **99B**, 257 (1981).
[34]F. Mane *et al.*, Phys. Lett. **99B**, 261 (1981).
[35]F. Mane *et al.*, Phys. Lett. **112B**, 178 (1982).
[36]A. Cordier *et al.*, Phys. Lett. **106B**, 155 (1981).
[37]J. Buon *et al.*, Phys. Lett. **118B**, 221 (1982).
[38]K. Abe *et al.*, Phys. Rev. Lett. **53**, 751 (1984).
[39]D. Aston *et al.*, Phys. Lett. **93B**, 517 (1980).
[40]Particle Data Group, C. G. Wohl *et al.*, Rev. Mod. Phys. **56**, SI (1984).
[41]J. Pumplin, Phys. Rev. D **2**, 1859 (1970).
[42]B. G. Gibbard *et al.*, Phys. Rev. Lett. **42**, 1593 (1979).
[43]D. P. Barber *et al.*, Phys. Lett. **90B**, 470 (1980).
[44]V. Chaloupka *et al.*, Phys. Lett. **61B**, 487 (1976).
[45]W. Brukner *et al.*, Phys. Lett. **67B**, 222 (1977).
[46]A. S. Carroll *et al.*, Phys. Rev. Lett. **32**, 247 (1973).
[47]P. Benkeirs *et al.*, Phys. Lett. **68B**, 483 (1977).